

Surface-based Smoothing of Brain Imaging Data in Voxel Space

DIPLOMARBEIT

Zum Erlangen des akademischen Grades
Diplom-Ingenieur
im Rahmen des Studiums Biomedical Engineering
E066 453

Ausgeführt am
¹Institut für Angewandte Physik
der Technischen Universität Wien

in Zusammenarbeit mit den
²Neuroimaging Labs
der Universitätsklinik für Psychiatrie und Psychotherapie
Medizinische Universität Wien

unter der Anleitung von
Ao. Univ. Prof. Dr. Martin Gröschl¹
Assoc. Prof. Dr. Andreas Hahn²

durch
Peter Stöhrmann
Matrikelnummer e01226992

Datum, Unterschrift (Student)

Datum, Unterschrift (Betreuer)

Hiermit erkläre ich, dass ich diese Arbeit selbständig verfasst, die verwendeten Quellen und Hilfsmittel vollständig angegeben und Stellen der Arbeit – einschließlich Tabellen, Karten und Abbildungen –, die anderen Werken oder dem Internet im Wortlaut oder dem Sinn nach entnommen sind, auf jeden Fall unter Angabe der Quelle als Entlehnung kenntlich gemacht habe.

Ort, Datum, Unterschrift

1 Abstract

Functional magnetic resonance imaging (fMRI) and positron emission tomography (PET) are two modalities used to assess human brain function in terms of neuronal activation, glucose metabolism or receptor binding. In fMRI, the blood oxygen level dependent (BOLD) signal is the most commonly employed approach to assess the neuronal response to certain stimulation.

For either method, the generally small measured signals result in a poor signal-to-noise ratio (SNR). Other limitations of these imaging techniques are the inverse relationship of spatial and temporal resolution, partial volume effects (PVE) and the complex anatomy and function of the brain itself. As a result, preprocessing is needed prior to statistical analysis of the acquired images, typically including spatial smoothing of data. Smoothing may be performed either in voxel space, that is three-dimensional smoothing, or along an inflated brain surface in two dimensions. Although both approaches increase SNR, they are subject to limitations on their own.

The advantages of smoothing in voxel space are its processing speed, low memory requirements, and ease of implementation in a computational pipeline. Its major disadvantage is given by the brain anatomy: the gray matter (GM) of the brain is adjacent to white matter (WM) and cerebrospinal fluid (CSF). Furthermore, gyration increases the brain's surface area, with functionally distinct areas being in close proximity.

Without further constraints, smoothing in voxel space is applied to the whole measured volume, though, resulting in a mixture of data from neighboring, but anatomically and functionally different tissues and gyri. In contrast to Euclidean, (i.e. linear), distances used in three-dimensional smoothing, geodesic distances describe the spacing of points along a surface or constrained path. Applied to the brain, distinct neuronal populations of adjacent gyri may be close in Euclidean space, but far apart by geodesic, and also functional means.

Smoothing along the triangulated and inflated brain surface, e.g. using heat kernels (an implementation of Gaussian smoothing), resembles geodesic-distance smoothing. However, this is computationally expensive, and errors may be introduced during surface extrapolation and inflation, and thus is rarely applied.

The aims of this thesis are i) to develop a novel smoothing procedure in voxel space using geodesic distances, ii) to directly compare different smoothing methods and iii) to assess their influence on SNR.

It will be shown that the novel approach called gQED (geodesic Quasi-Euclidean Distance smoothing) performed similar to a reference (SPM) in terms of detection of neuronal activation and SNR but additionally allowed for smoothing within well-refined masks which may increase spatial specificity. The use of such masks on group-level, though, requires higher spatial normalization quality than commonly used. gQED smoothing is slower than the volumetric smoothing method, but a complete volumetric analysis with gQED including all other necessary preprocessing steps is still much faster than surface-based analyses. Therefore, the approach provides a more anatomically and physiologically correct alternative to current three-dimensional smoothing, while maintaining computational efficiency as compared to surface smoothing.

2 Kurzfassung

Funktionelle Magnetresonanztomographie (fMRT/fMR) und Positronen-Emissions-Tomographie (PET) werden häufig zur Evaluierung von Hirnaktivität angewandt. Damit können beispielsweise die neuronale Aktivierung, Glukosestoffwechsel oder die Bindung von Rezeptoren untersucht werden. Bei der fMRT wird am häufigsten das von der Hämoglobinoxxygenierung abhängige BOLD-Signal verwendet, um die neuronale Reaktion auf spezifische Stimulation zu untersuchen.

Die gemessenen Signale besitzen im allgemeinen geringe Intensität, was zu einem niedrigen Signal-Rausch-Verhältnis (SNR) führt. Weitere Einschränkungen der oben genannten Bildgebungsmodalitäten sind das inverse Verhältnis von zeitlicher und räumlicher Auflösung, der Teilvolumeneffekt, und nicht zuletzt die komplexe Anatomie und Funktion des Gehirns.

Daraus resultiert die Notwendigkeit der Prozessierung vor der statistischen Auswertung, die meist auch räumliches Glätten der Daten beinhaltet, welches entweder im 3-dimensionalen Raum oder entlang der entfalteten Hirnoberfläche in nur zwei Dimensionen durchgeführt werden kann. Beide Herangehensweisen erhöhen die SNR, besitzen aber auch Nachteile. Vorteilhaft an der 3D-Prozessierung ist die hohe Geschwindigkeit, einfache Implementierung und geringes Speicheraufkommen. Der größte Nachteil ergibt sich durch die Anatomie des Gehirns, bestehend aus weißer und grauer Substanz, sowie zerebrospinaler Flüssigkeit, und den Hirnwindungen wodurch funktionell unterschiedliche Regionen räumlich eng beieinander liegen.

Ohne weitere Einschränkung wird die 3D-Glättung aber auf das gesamte aufgenommene Volumen angewendet, wodurch Signale aus räumlich benachbarten aber funktionell unterschiedlichen Geweben und Hirnwindungen vermischt werden. Im Gegensatz dazu steht die Verwendung geodätischer Distanzen, gemessen entlang einer Oberfläche oder entlang eines eingeschränkten Pfades. Diese werden bei der Glättung entlang der entfalteten, triangulierten Gehirnoberfläche verwendet. Der Prozess der Triangulation und Entfaltung sowie die anschließende Glättung erfordern jedoch viel Zeit, Speicherplatz und Rechenaufwand und sind keine fehlerfreien Algorithmen. Deshalb wird nach wie vor bevorzugt die volumetrische Glättung angewandt.

Die Ziele dieser Diplomarbeit sind i) die Implementierung eines neuartigen Glättungsprozederes unter der Anwendung von geodätischen Distanzen im dreidimensionalen Raum, ii) einen direkten Vergleich zwischen unterschiedlichen Glättungsmethoden herzustellen und iii) deren Einfluss auf das Signal-Rausch-Verhältnis zu untersuchen.

Es wird gezeigt, dass die neue als gQED bezeichnete Methode ähnlich gute Resultate liefert wie gängiges volumetrisches Glätten, mit korrekter Maskierung dabei aber höhere räumliche Spezifität möglich ist. Die dafür benötigten Masken lassen sich für Gruppen-Statistiken allerdings nur anwenden, wenn besonders gute räumliche Normalisierung erreicht wurde. gQED ist langsamer als andere räumliche Glättungsmethoden, der gesamte Analyse-Prozess ist jedoch dennoch deutlich schneller als oberflächenbasierte Auswertungen.

Dieser Ansatz bietet daher eine anatomisch und physiologisch genauere Alternative zur gängigen 3D-Glättung, unter Erhaltung der einfachen Implementierung und rechnerischen Effizienz.

3 Acknowledgements

I want to express my gratitude to Prof. Martin Gröschl, who kindly offered to supervise my diploma thesis.

I am thankful for Assoc. Prof. Rupert Lanzenberger welcoming me at the Neuroimaging Labs (NIL) and providing me with the opportunity to combine my love for physics and medicine. Special thanks to Assoc. Prof. Andreas Hahn who acted as my co-supervisor and mentor, and all my colleagues who did not get tired answering my questions and who provided me with their study data and shared their expertise.

Prof. Gerald Badurek and Dr. Albert Hirtl whose lectures on magnetic resonance imaging and functional imaging deeply influenced me shall also not be forgotten.

Last, but not least, I want to thank my wife as well as her and my family for their never-ending encouragement, their patience and support.

Table of Contents

1	Abstract	3
2	Kurzfassung.....	4
3	Acknowledgements	5
4	Motivation and Aim	9
5	Background	10
5.1	Imaging Modalities	10
5.1.1	MRI	10
5.1.2	BOLD fMRI.....	12
5.2	Preprocessing	13
5.2.1	Slice Time Correction	13
5.2.2	Realignment – Motion Correction.....	14
5.2.3	Coregistration	14
5.2.4	Spatial Normalization.....	14
5.2.5	Spatial Smoothing	14
5.2.6	Statistics – GLM.....	15
5.3	Noise	16
5.3.1	Physiological Noise.....	17
5.3.2	SNR.....	17
5.4	Brain Anatomy – Motor Cortex	18
6	Methods.....	20
6.1	Simulated Data	20
6.2	Smoothing	21
6.2.1	Convolution.....	21
6.2.2	SPM.....	21
6.2.3	gQED.....	22
6.2.4	Comparison in 1D	24
6.2.5	Comparison in 3D	25
6.2.6	Adaptive Smoothing.....	27
6.2.7	Surface Based Analysis – FreeSurfer/FS-FAST	27
6.3	Experimental Data.....	28
6.3.1	Population.....	28
6.3.2	Measurement	29

Surface-based Smoothing of Brain Imaging Data in Voxel Space

6.3.3	Volumetric Analysis.....	29
6.3.4	Surface-Based Analysis.....	30
6.3.5	Statistics	31
7	Results	32
7.1	Artificial Data.....	32
7.1.1	Single Subject.....	32
7.1.2	Group Statistics	34
7.2	Volumetric Experimental Data.....	34
7.2.1	Single Subject.....	34
7.2.2	Spatial Normalization.....	37
7.2.3	Masking.....	39
7.2.4	Group Statistics	39
7.3	Surface-Based Experimental Data.....	40
7.3.1	Single Subject.....	40
7.3.2	Group Statistics	41
8	Discussion	42
8.1	Normalization.....	42
8.1.1	GM Overlap.....	43
8.1.2	Spatial Signal Separation	43
8.2	Smoothing	43
8.2.1	Masking and Crosstalk	43
8.2.2	Signal Magnitude and Variability	44
8.2.3	Activation Detection and Localization.....	45
8.2.4	Computational Performance.....	45
8.3	Limitations	46
8.3.1	Masking.....	46
8.3.2	CVS-Normalization.....	46
8.3.3	Software - Licenses	47
8.4	Other Smoothing Approaches	47
8.4.1	Anatomically Informed Basis Functions.....	47
8.4.2	Gaussian Processes.....	47
8.5	Possible Enhancements and Outlook	48
8.5.1	Computation Time and Memory Requirements.....	48

Surface-based Smoothing of Brain Imaging Data in Voxel Space

8.5.2	Further Applications.....	49
9	Conclusion.....	51
10	References	52
11	Table of Figures	56
12	Appendix	59
12.1	Acronyms and Abbreviations.....	59
12.2	Code	60
12.2.1	Intracortical (Geodesic) Distances	60
12.2.2	gQED Smoothing	63

Die approbierte gedruckte Originalversion dieser Diplomarbeit ist an der TU Wien Bibliothek verfügbar.
The approved original version of this thesis is available in print at TU Wien Bibliothek.

4 Motivation and Aim

In neuroscience, neurology and related fields, accurate localization of neural activity is fundamental for understanding brain function as well as for treatment planning.

Especially in surgery, already small spatial deviations of a few millimeters from the true site of activation can make the difference between life-long impairment or full recovery. Also in research, small localization errors may result in activation being attributed to a different brain region with substantially different function.

The reasons for difficulties in localization are manifold, some of which are even voluntarily introduced through data processing such as smoothing, others are rooted in the nature of the signals, brain anatomy or limits to image resolution. Spatial smoothing is commonly used to improve the signal-to-noise ratio (SNR) of the acquired image, both increasing statistical power and to facilitate identification of neuronal activation. It is useful for the application of the general linear model (GLM) which is often used for statistical analysis, as errors will show a Gaussian distribution. When analyzing groups, smoothing also reduces any anatomical variation that may still be present after spatial normalization.

While the necessity of smoothing cannot be denied, some smoothing procedures such as volumetric smoothing with a Gaussian kernel may introduce severe limitations. These have been known and investigated for many years, see e.g. [1]: Signals from different, adjacent tissues may be mixed or falsely “transferred” to spatially close, yet functionally distant and uninvolved brain regions. Smoothing may also introduce shifts in the location of maxima in the same brain region and distortion of the activated area.

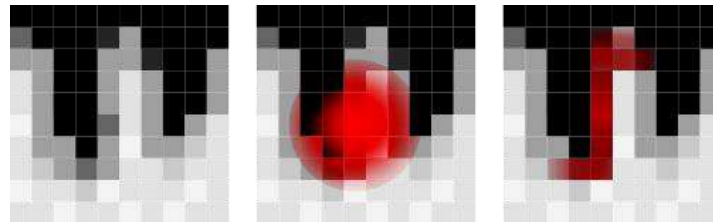


*Fig. 1 Schematic description of spatial smoothing: **left**: exemplary gyri (GM: dark gray, WM: light gray) and sulci (CSF: black), **middle**: smoothing by Euclidean distance as most commonly used, **right**: smoothing by geodesic distance as proposed in this work.*

Numerous alternative procedures have been introduced with the aim of reducing localization errors, but these have limitations of their own. Since volumetric smoothing is easily applicable, implemented in many processing programs, needs less memory and is typically faster than its substitutes, it is still most commonly applied.

The aim of this work is to introduce a novel voxel-wise smoothing procedure which takes into account the anatomy of the brain and thus offers smoothing solely across the gray matter surface. This reduces the shortcomings of Gaussian, volumetric smoothing while preserving its advantages of computational efficiency. The algorithm’s performance is then compared with commonly used alternatives.

5 Background

In the following pages the reader will be introduced to the basics of (functional) image acquisition, image preprocessing and statistical analysis. For a more thorough treatise the interested reader may be referred to the vast amount of literature covering this topics, such as [2], [3] and [4] from which the following information is derived, if not stated otherwise.

5.1 Imaging Modalities

Nowadays, many different anatomical and functional imaging modalities exist such as X-rays, computed tomography (CT), magnetic resonance imaging (MRI), single-photon computed tomography (SPECT) and positron emission tomography (PET). In contrast to anatomical images where the structure and spatial extent of organs is captured, functional imaging captures physiological processes, often over a period of time. Depending on the method these observations can range from the macroscopic down to the molecular level. Although functional brain imaging is by far not limited to fMRI, this thesis uses fMR data (specifically BOLD-signals) as an example. It has to be kept in mind, though, that preprocessing and smoothing are also applicable to other modalities (e.g. PET) and that the proposed smoothing method is invariant of the imaging modality and that observations on the resulting data can be transferred to other methods.

Before discussing image formation, a short remark on visualization conventions is necessary: Axial brain slices can be regarded from below as if standing at the foot end of the patient's bed (radiological convention) or from above as if standing behind the sitting patient and looking down on her/his head (neurological convention). These two options can cause confusion as the hemisphere on the left of an axial or coronal image can be either the patient's left (neurological convention) or right hemisphere (radiological convention). In this work the radiological convention is used, as also indicated by letters next to the slice images denoting anatomical directions.

5.1.1 MRI

In magnetic resonance imaging, the subject is placed in a strong, uniform, stationary magnet field B_0 , which causes the spins of unpaired protons (equivalent to hydrogen nuclei) within the subject to reorient and precess along B_0 with the Larmor frequency

$$\omega_0 = \gamma_p B_0 \quad (1)$$

where γ_p is the gyromagnetic ratio of a proton (a constant).

In clinical applications B_0 is typically 1.5 or 3 T (Tesla¹), whereas 7 T is getting more available for research. The spins can be macroscopically described by magnetic dipoles. A radiofrequency (RF) impulse is used to perturb the aligned spins, rotating them and their magnetization M vector towards the transverse plane.

As can be seen in eq. (1), the Larmor frequency and thus the RF to be used depend on the local magnetic field strength. In order to only perturb a certain slice within the subject, a gradient field is applied. As the spins gradually realign along B_0 , they lose energy and the measurable signal slowly decays. Put into formulae we can describe the precession by

$$\frac{d\vec{M}}{dt} = \gamma_p \vec{M} \times \vec{B}_0 \quad (2)$$

¹ 1 T = 1 $\frac{kg}{As^2}$ = 1 $\frac{Vs}{m^2}$

Denoting M 's component parallel to B_0 as $M_{||}$, after the RF-pulse $M_{||}$ will exponentially gain its original magnitude M_0 , with a time constant T_1 , also called longitudinal relaxation time.

$$M_{||} = M_0 \left(1 - e^{-\frac{t}{T_1}} \right) \quad (3)$$

The spins also exhibit their own interactions (spin-spin interactions) causing dephasing of their (during the RF-pulse synchronized) precession with time constant T_2 . This reduces M 's normal net component M_{\perp} exponentially:

$$M_{\perp} = M_0 e^{-\frac{t}{T_2}} \quad (4)$$

For spatial encoding in the xy -plane, especially using the sophisticated phase encoding the reader may be referred to literature.

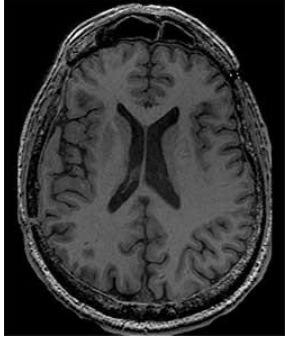
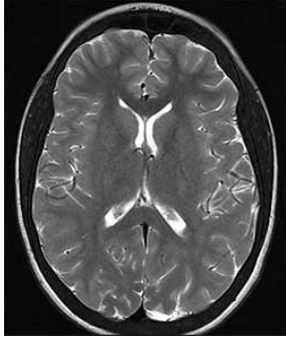
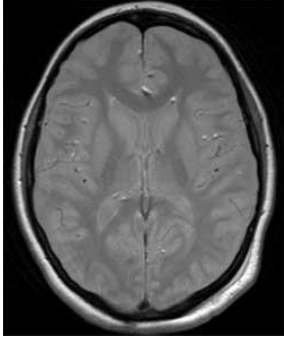
	T1	T2	PD (Proton Density)
Weighting	Max T1 contrast shown	Max T2 contrast shown	Proton density/ H nuclei density shown
Image			
Water signal	Water has a long T1. T1-weighted imaging (WI) uses a short TR so the signal from water is still low, therefore, water appears dark	T2-WI uses a long TE so the signal from water is high, therefore, water appears bright	A long TR results in a high water signal, but a short TE means that this is less than the signal of a T2 scan. The signal of water is in the middle
Fat signal	Fat has a short T1, so even though the TR is short the signal is still high and fat appears bright	Fat has a short T2, so at a long TE the signal is less bright and it will be darker than water, but still high	A long TR results in a high fat signal, and short TE means this signal is higher than on a T2-WI. Fat appears bright
TR (repetition time)	Short. 300-600 ms	Long. 2000 ms	Long. 1000-3000 ms
TE (echo time)	Short. 10-30 ms	Long. 90-140 ms	Short. 15 ms

Table 1 Difference between T1-, T2- and PD-weighted images of the brain, reproduced from [5]

T_1 - and T_2 -weighted images are used for different clinical applications, as e.g. discrimination of tissue types varies between them (see Table 1). T_2^* which may also be seen when discussing MRI acquisition, describes the actually measured spin dephasing due to field inhomogeneities within the scanner. T_2^* is shorter than T_2 . The 'real' T_2 can be measured indirectly by echoing (180° RF pulses), which causes the spins to temporarily rephase.

In general

$$T_2^* \leq T_2 \leq 2 T_1 \quad (5)$$

Two further important time measures are TR (repetition time), the time between RF pulses and TE (echo time), the time between echo RF pulses. T_1 and T_2 are tissue properties, whereas TE and TR are set during image acquisition and have a major influence on the measured signal intensity.

Signal intensity S has been found to be approximately described by a constant K multiplied with the tissue's proton density $[H]$ and two terms representing the relationship of TR/ T_1 and TE/ T_2 . $[H]$, T_1 and T_2 can be assumed constant at a specified tissue location, thus the measured signal and reconstructed image depend solely on the choice of TE and TR as described in Eq. (6)

$$S \approx K \cdot [H] \cdot \left(1 - e^{-\frac{TR}{T_1}}\right) \cdot e^{-\frac{TE}{T_2}} \quad (6)$$

The effects of varying TE and TR and the resulting T1- and T2-weighted images are displayed in Table 1.

5.1.2 BOLD fMRI

Functional MRI is based on the aforementioned processes but is used to describe physiological processes such as perfusion and indirectly brain activity. A common fMRI-method employed is based on the paramagnetic, signal-weakening properties of deoxygenated hemoglobin, aptly called BOLD-signal (blood oxygen level dependent). A local increase in neural activation will lead to higher oxygen consumption resulting in more deoxygenated hemoglobin (corresponding to the – not always visible – initial dip of the signal). This, though, is overcompensated by increased perfusion, leading to a lower net ratio of deoxygenated blood in this area and a higher T_2^* signal. The signal variation is described by the hemodynamic response depicted in Fig. 2 (top left). The BOLD-signal change is in the order of only a few percent of the total signal.

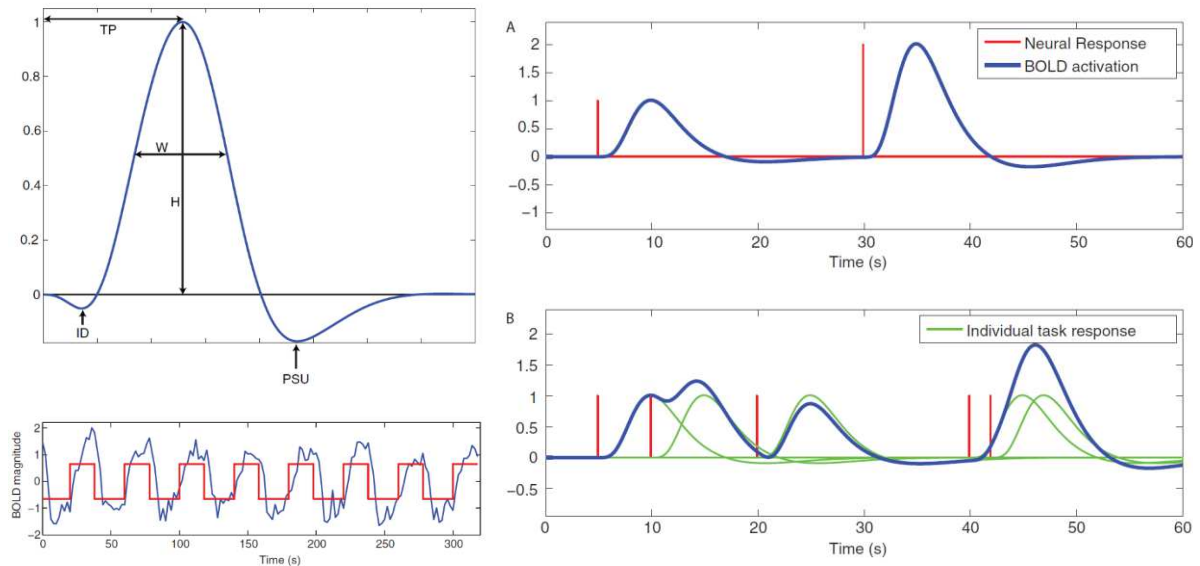


Fig. 2 **Top left:** hemodynamic response function (HRF) schematic: ID ... initial dip; TP ... time from stimulus to peak; W ... width at half height; PSU ... post-stimulus undershoot ; **Lower left:** BOLD fMRI series: stimulus (red) and corresponding response (blue); **Top right:** Signal for different neural response magnitude; **Lower right:** Approximately linear response of BOLD for several stimuli within short time interval; Composition of several figures from [4]

BOLD activation correlates with the magnitude of the neural response and adds up for events in quick succession (Fig. 2 lower right). The time course of blood oxygen levels for sequentially continuous activity is also depicted (Fig. 2 bottom left). It relates to activity provoked by task performance or application of continuous external stimuli during well-defined time-intervals (i.e., the experimental paradigm).

This time course can be estimated by convolution of a single HRF with a design vector corresponding to the task/stimulus. Many different approaches to model the HRF exist, though. Common choices are a single gamma function (canonical HRF) and the difference of two gamma functions, also modelling the post-stimulus undershoot. Inter- but also intra-subject variability of the HRF led to the development of more complicated but flexible models, e.g. using different basis sets. There is a trade-off, though, between flexibility of HRFs (less flexible functions being more biased as they only model close matches of a single HRF) and variability of the resulting estimates. [4]

For cognitive tasks, several well-timed repetitions with pauses in-between allows for more powerful estimates of the neural activation in the corresponding brain regions. For the detection of (de-)activated brain regions in correspondence with the paradigm the reader is referred to section 5.2.6.

Opposed to the just now described task-based fMRI is resting-state fMRI, where subjects are asked to lie still and let their mind roam freely. Time courses of several regions of interested are then tested for temporal correlation which is used as a metric of functional connectivity.

5.2 Preprocessing

5.2.1 Slice Time Correction

MR and fMR images of brain volumes are commonly acquired in consecutive or interleaved slices, e.g. when using echo-planar sequences (EPI). The repetition time TR for fMR images of the whole brain is in the order of two seconds, meaning that all slices of a volume will be acquired within one TR. This results in a delay between the different slices up to

$$\Delta t = TR - \frac{TR}{n} \quad (7)$$

seconds later and a subsequent signal loss as shown in Fig. 3. To avoid false negatives in functional analysis it is therefore necessary to correct for the time point of slice acquisition and to simulate simultaneous acquisition of the whole volume.

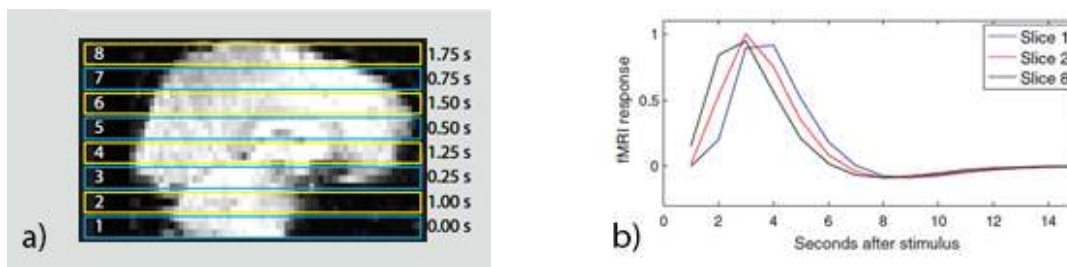


Fig. 3 Slice Time Correction: a) slice order for interleaved acquisition; b) corresponding signals; Later acquired slices appear to exhibit an earlier response, as they do not detect the true onset of the HRF; Taken from [4]

5.2.2 Realignment – Motion Correction

fMRI data is used to describe the time course of the neuronal response. Thus, a continuous series of images is acquired (one with each TR), which may however be corrupted by subject motion. Correction for patient movement, both within time frames, as well as from one frame to another, is crucial to accurately localize activation. Within-frame movement can only be suppressed by restricting the patient's ability to move. Frame-to-frame movement can be compensated before statistical analysis by performing spatial transformations and registering the frames, during which rigid transformations are applied with six degrees of freedom (three translations, three rotations). Typically, either one selected frame (first or middle) or a mean image is used as a reference to which the other frames are then brought into alignment.

5.2.3 Coregistration

Coregistration describes the process of spatially matching volumes from different imaging modalities or different measurements. Transformations for coregistration thus may also include scaling and shearing to compensate for differences in measured volume, resolution and orientation. fMR images contain little anatomical information. To accurately localize an activated region, they need to be coregistered to a structural MR image.

5.2.4 Spatial Normalization

For inter-subject comparison and group analyses the images need to be spatially normalized, to match an anatomy template in standardized space. As some brain structures exhibit large variability, this may only be partially possible. For normalization, atlases such as MNI152 (Montreal Neurological Institute) are used, which include averaged data from large populations (in that case 152 subjects). Normalization, coregistration and even realignment depend on cost functions such as least-squares, (normalized) correlation or mutual information. These describe the degree of alignment. The better the match, the smaller the cost function, which is minimized iteratively.

For group analysis it has to be kept in mind, that using 3D normalization of the whole brain may not generally result in well-overlapping cortices and gyri of different subjects [6]. Surface-based registration theoretically promises better alignment which proves advantageous in group-level statistics but requires individual surface maps and typically excludes deeper brain structures. [7]

Few hybrid methods such as CVS (combined volume and surface morph) [8] also exist. These model the gyration of the brain like surface-based approaches but instead of 'inflating' the surface to a sphere they apply transformations to match the surface and whole volume to a standardized brain template, resulting in alignment of cortical and subcortical regions in 3D voxel space.

When data of several subjects is compared in template space (instead of referring to anatomical landmarks) or used for group statistics, the same anatomical structures in different subjects should overlap as well as reasonably possible. Even in healthy and demographically matched cohorts (age, sex/gender, handedness...) this may be a challenging task as sulci still may vary in location and depth. This reduced spatial match can negatively influence detection of spatially small brain activity.

5.2.5 Spatial Smoothing

As previously stated, smoothing may serve multiple purposes in data analysis, such as increasing activation detection sensitivity, reducing normalization errors and intersubject anatomical

variability, increasing SNR and allowing the use of statistical models (see section 5.2.6). Smoothing also changes data in undesired ways, though: Spatial resolution and specificity are reduced (at least for non-adaptive smoothing), false positives may be introduced, activation regions are likely to be inflated and information on their shape and spatial extent is reduced [9]. Even shifts of activation may be introduced, as described e.g. by [10]. When optimizing the size of the kernel, the positive aspects should outweigh the disadvantages of smoothing. Kernel optimization is commonly omitted, though, and default values or values following rules of thumb are used.

5.2.5.1 Smoothing Introduced by Other Preprocessing Steps

A low level of smoothing is also introduced involuntarily by all pre-processing steps using spatial and/or temporal interpolation of the signal. Since these steps include spatial transformations of the brain both within the original space (realignment) as well as changes in the size of the voxels and of the analysis volume, a comparison of time courses of a single voxel after each preprocessing step is not sensible to implement. Thus, noise was only compared for two instances in the preprocessing pipeline: after normalization and after smoothing.

5.2.6 Statistics – GLM

Once the previously explained steps have been completed data can be exploited in search of (de-) activation patterns matching the experiment and/or correlation between activity of different brain areas.

In a mass univariate analysis, the time course of each voxel's intensity (Voxels are "VOLumetric piXELs", i.e. the 3D-analogue of pixels) will be modelled and compared to the time course of external stimuli or tasks. Thus, (de-)activation does not simply imply a large signal or a signal increase, but a change in BOLD-signal in accordance with the experiment's time course.

For task-based fMRI, the general linear model (GLM) is the most common statistical analysis method (Eq. (8)). For a visualization of the GLM see Fig. 4.

$$Y = \tilde{X} \cdot \beta + \epsilon \quad (8)$$

The measured BOLD-signal of a single voxel (Y in eq. (8)) is estimated by the expected response time-course (design matrix \tilde{X}), multiplied with weights β plus an additional error term (residuals) ϵ . The design matrix includes regressors of interest, representing a convolution of the HRF with the occurrence of stimuli, and nuisance regressors (covariates) modelling subject motion and include a constant for signal offset and drift. Tissue regressors (e.g. mean time course in white matter) may additionally be used to remove unspecific signal changes that affect the whole brain.

β -values, representing the "importance" of a regressor in the measured signal, are then tested for significance.

The GLM is based on two major assumptions: 1) Errors are random, independent and follow a Gaussian distribution with zero mean and 2) the HRF linearly correlates to the neuronal signal. Unfortunately, though, both are violated, as BOLD-signals exhibit a large degree of auto-correlation and the neuronal response in some cases may differ significantly from linear behavior. A detailed discussion on these issues and how they can be corrected can be found in [4] and [11].

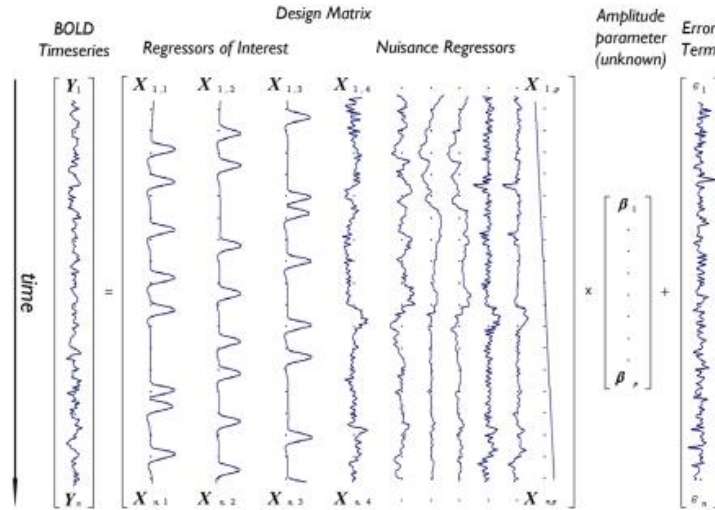


Fig. 4 GLM-schematic taken from [11]: A BOLD time-course is predicted by three tasks and seven nuisance regressors

5.3 Noise

In (f)MRI the term noise is unfortunately inconsistently used. In the context of his thesis “noise” shall refer to the sum of (temporal) data variability σ not deliberately introduced by the experimental design. A major component of noise is thermal noise σ_T introduced during image acquisition (Johnson-Nyquist noise), whose source is mainly the subject itself. The next largest contribution to thermal noise is electronic noise in the receiver. Various noise modeling approaches exist, considering differences in image modality, acquisition (coil systems used), reconstruction and further processing.

A commonly used assumption for thermal noise in image domain (k-space) is a zero-mean, spatially uncorrelated Gaussian process. Variance in imaginary and real parts are presumed to be equal. In the spatial domain (x-space), this results in models following a Rician distribution for single-coil systems and noncentral- χ (nc- χ) distribution for multiple-coils (see Fig. 5). Special attention needs to be paid when using modern acquisition-accelerating procedures, which e.g. rely on subsampling, as they alter noise.

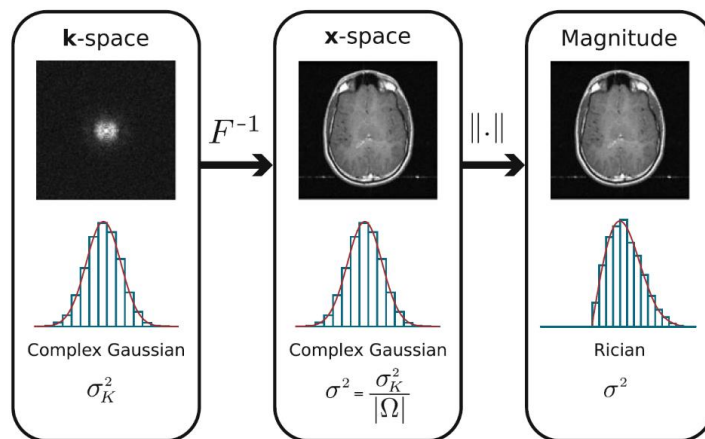


Fig. 5 Noisy image: left to right: data acquisition to final image; σ^2 ... Variance; $|\Omega|$... Size of Field of View (number of points in 2D inverse discrete Fourier transform); For large SNR the signal can be estimated as Gaussian distributed, for SNR = 0 (i.e. image background) the Rician distribution simplifies to a Rayleigh distribution; Taken from [12]

Noise removal is a controversial topic within the imaging community and depends on aforementioned noise estimates and the purpose of filtering. Denoising methods are not limited to signal estimation but may be also performed via wavelets (similar to Fourier-analysis) or non-local means (means of voxels with similar surroundings). [12]

5.3.1 Physiological Noise

Head motion, heartbeat (pulsatile blood flow), breathing, and other variable physiological processes will introduce physiological noise σ_P during imaging. The two former play an especially important role in imaging of deep brain structures. (Partial) removal of physiological noise during data analysis is possible by independent component analysis (ICA) or if heartbeat and breathing have been monitored during measurement via modelling or gated image acquisition (i.e. only during a specified time interval of the heart cycle). [12]

Physiological noise is the only signal-strength dependent noise contribution and may even account for most of to the SNR. It can be further characterized as the sum of fluctuations in transverse relaxation rate σ_B (related to BOLD-associated processes) and σ_{NB} , describing cardiac and respiratory as well as non-TE-related scanner influences. [13]. Different contributions to overall noise are shown in Fig. 6.

5.3.2 SNR

The signal-to-noise (SNR) ratio is defined as the fraction of signal S and total image noise σ :

$$SNR = \frac{S}{\sigma} \quad (9)$$

where

$$\sigma = \sqrt{\sigma_T^2 + \sigma_S^2 + \sigma_P^2} \quad (10)$$

and σ_S summarizes system noise including drift as well as shimming (the process of making the field more homogenous by running current through additional coils), field and RF imperfections.

A large signal-to-noise ratio requires a preferably large signal compared to the approximately constant noise, and is correlated to measurement parameters such as repetition time TR, echo time TE, voxel volume ($SNR \propto V_{vox} \propto \Delta x \cdot \Delta y \cdot \Delta z$ for a constant field of view) and number of excitations (resulting in a mean image of lower noise). In fMRI, varying the latter is typically beyond the influence of the technician, due to the changing signal over time. For details on the effect of resolution on SNR the reader is referred to [14].

As can be seen in Fig. 6, physiological noise is significantly larger in GM, than in WM. [13]

In later analyses temporal SNR will be estimated by using the (GLM-)estimated time course ($\mathbf{Y} = \tilde{\mathbf{X}} \cdot \boldsymbol{\beta}$) of a single activated voxel as pure signal and the residuals (difference of modeled HRF and real time course) as noise. It has to be stressed, though, that this is not the only option to estimate temporal SNR. An alternative approach would be to use resting periods and locations where little variation in neural activity is to be expected.

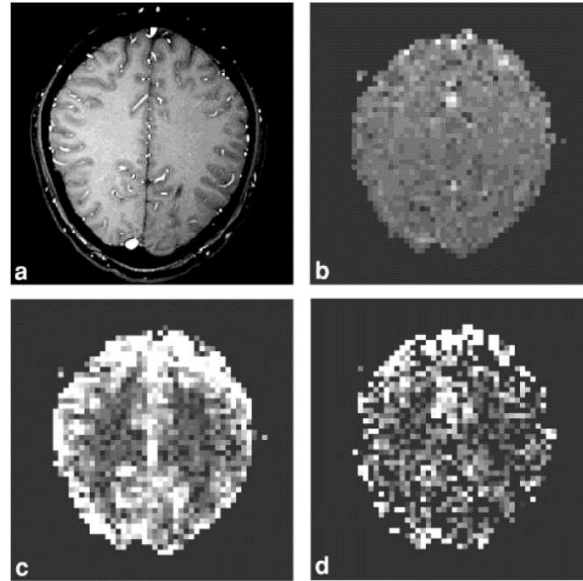


Fig. 6 Noise contributions as depicted and described in [13]: “Anatomy (a) and spatial distribution of raw noise σ_0 (b), physiological noise contributions σ_B (c), and σ_{NB} (d) in a typical image section from one subject. Note that gray scale contrast is identical in b–d.”

5.4 Brain Anatomy – Motor Cortex

Functional imaging of the brain aims to identify stimulation-induced neuronal activation and to link this to the underlying anatomical structures. Since this will be relevant to discuss the chosen approach and data presented in this thesis work, a short overview on the motor cortex will be given below:



Fig. 7 Location of left motor hand area on the MNI152 template, localized as described in [15]: “The segment of the precentral gyrus that most contained motor hand function was a knob-like structure, that is shaped like an omega or epsilon in the axial plane and like a hook in the sagittal plane.”

While no brains look the same, in normal healthy brains the same (relative) locations are roughly linked to the same discrete functions, especially when it comes to motor control (see e.g. Fig. 7). On subject level these can be localized with either invasive methods such as electro-stimulation and more commonly employed non-invasive methods and imaging modalities. In the beginnings of neuroscience head and brain injuries and resulting cognitive and/or motor deficiencies were also important indicators for the linkage between anatomy and function.

Motor activity (planning, execution and control) is associated with the motor cortex. The primary motor cortex is part of the dorsal frontal lobe (see Fig. 8) and can be divided in brain regions

responsible for movement of different body parts. These can be visualized with the help of a distorted body drawn on the cortical surface, called homunculus ('little person'). The homunculus along with a wide variety of anatomical and functional atlases may be used as a reference in the analysis of fMRI data.

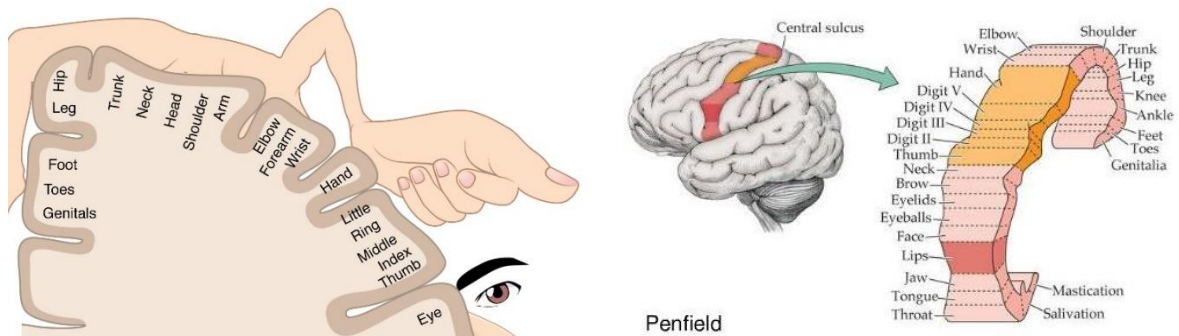


Fig. 8 Primary motor cortex: Sensory homunculus: **Left:** Coronal view (Source: [16]) **Right:** Lateral view, Penfield's map (Source: [17])

6 Methods

6.1 Simulated Data

To test the different smoothing algorithms in an environment with known ground truth artificial fMR images were used with well-defined parameters such as known SNR and well-defined activation location, underlying HRF and time course (event onset and duration and signal drift). This is a common approach in analysis and debugging of processing algorithms. Unfortunately, though, unpublished in-house code is often used for this purpose and only few well-established models are publicly available. For a thorough review on fMRI simulations see e.g. [18]. All of the artificial data did not require any preprocessing steps prior to smoothing. There is no movement of the ‘brain’ and the whole brain can be ‘imaged’ simultaneously, thus there is no need for slice time correction or realignment.

The artificial data for this thesis was created pursuing two separate approaches:

As a first step an interpolated HRF was convolved with a binary design-matrix, resulting in the seed-voxel’s time course (see Fig. 9). This represents a local task-related neural activation. The spatial extent of the signal was derived by weighting the signal according to its anatomical distance to the seed in an idealized brain template. Noise was added to the whole volume and for all time points.

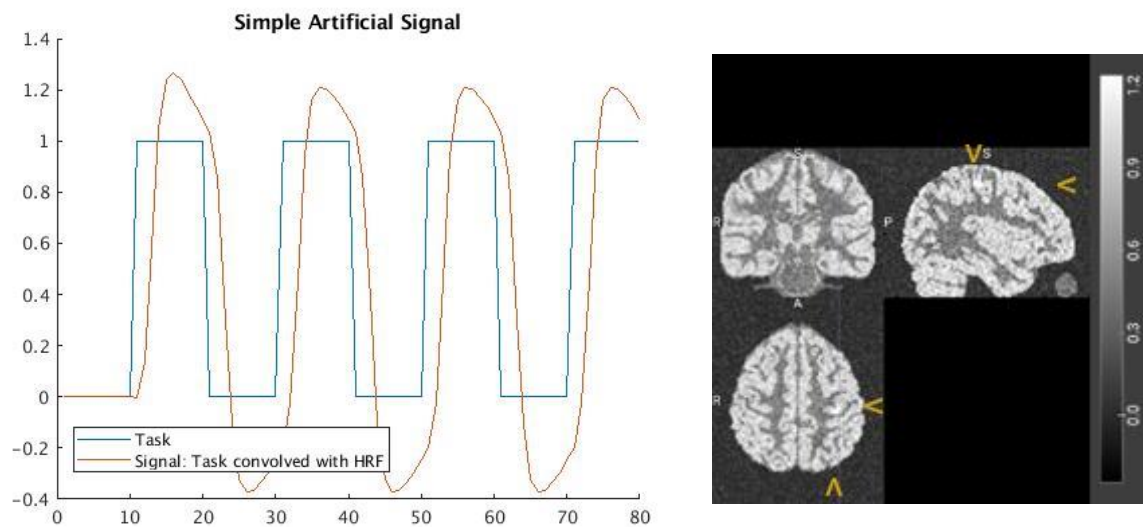


*Fig. 9 Artificial signal created by convolution of HRF and design matrix (‘Task’). **Left:** time course; **Right:** Single frame (time instance) of the resulting simulated BOLD-measurement shown in coronal, sagittal and axial slices. Activation (increased simulated BOLD-values) is slightly visible in the brain’s left hand-motor center as a small white batch of higher intensity than the surrounding tissue, the location is indicated by arrows.*

The second approach used a script based on code generously provided by J. R. Manning [19] and introduces more life-like variability and unknowns to the signal. With this script two studies were simulated: The first group-study used the same mask and seed as before. For the second study, brain masks were derived from real anatomical scans of different subjects. For each of the 20 subjects the location of the motor hand area was manually estimated on normalized anatomical scans as depicted in Fig. 7. GM-masks were made for each of the real subjects and an artificial BOLD-signal was initiated within a random voxel that coexisted in the GM-mask and a 5x5x5

voxel volume with the hand motor areas' coordinates as its center. This procedure guaranteed that inter-subject artificial activation varied to some extent but still matched corresponding brain regions as it was the case for the experimental data.

Afterwards, the simulated data was spatially smoothed with the following approaches.

6.2 Smoothing

Many smoothing algorithms rely on convolution of the image with a chosen function (smoothing kernel, commonly a Gaussian or similar function) or convolution analogs such as diffusion.

It shall be brought to the reader's attention, that surface (i.e. node-wise) and volumetric (voxel-wise) statistics do not differ, but any topological activation differences are mainly related to differences in spatial normalization and smoothing.

For a discussion on the topic of smoothing kernel size the reader shall be referred to literature, e.g. [20], [21] and [22]. A commonly applied rule of thumb is, that the FWHM (Full Width Half Maximum = span between values on opposite sides of the function's maximum with half the maximum intensity) should be at least twice the voxel size. A too large kernel, though, will also suppress true activation signal (matched-filter theorem).

6.2.1 Convolution

A comprehensive treatise of convolution with explanatory step-by-step MATLAB (Natick, Massachusetts: The MathWorks Inc.) code can be found in [23]. In short, convolution combines two signals (image and kernel) to a third with shared characteristics, by "smearing" one across the other. The process of "smearing" is implemented by shifting the signals with respect to each other and calculating their dot product.

For two continuous functions $f(t)$ and $g(t)$, the convolution is defined as

$$(f * g)(t) \stackrel{\text{def}}{=} \int_{-\infty}^{\infty} f(\tau)g(t - \tau)d\tau \quad (11)$$

The convolution w of two vectors u and v is mathematically described by

$$w = u * v \quad (12)$$

$$w(k) = \sum_j u(j)v(k - j + 1), \quad \forall j, k, k - j + 1 > 0 \quad (13)$$

6.2.2 SPM

The wide-spread MATLAB toolbox SPM12² (Statistical Parametric Mapping) offers built-in volumetric smoothing and is among the most used analysis tools for functional imaging [24]. It is well-established, has a large community, is quickly installed and easy to use without prior (programming) knowledge, making it a popular choice for neuroscientists. Therefore, it was chosen as the main reference in this thesis.

SPM performs unrestricted volumetric smoothing of the whole image with a kernel of constant size and without taking tissue borders and brain gyration into account. Independent of their functional and anatomical relationship the signals of two voxels get mixed with their Euclidean distance as only variable.

² For all computations in this thesis referring to SPM, SPM12: v6225 was used unless stated otherwise.

As default, the smoothing kernel is a Gaussian convolved with a first-degree B-spline with 8 mm FWHM. The kernel is thresholded to 6σ and normalized to sum to 1. Continuity of the underlying function is also accounted for. The convolution of the image with the kernel applies zero-padding in xy-plane and truncation along z as boundary conditions. For isotropic FWHM and sufficient distance to the border of the volume, smoothing along all axes can be considered the same. Especially for small FWHM, though, the kernel differs significantly from a pure Gaussian kernel regarding the function's flanks' steepness.

6.2.3 gQED

The smoothing modality proposed in this thesis uses Gaussian-weighted means based on geodesic Quasi-Euclidean Distances and will be abbreviated as gQED in this context.

As stated above Gaussian smoothing uses Euclidean distances. The length of a straight line connecting two points is a measure of the mutual influence of their corresponding signals during smoothing. While simple to implement and commonly used, this procedure lacks any consideration of brain anatomy and physiology. In contrast, the aim of gQED is to constrain the image volume based on brain anatomy and thus to smooth only within and along the gray matter:

As a first step, a mask is specified which includes the areas of interest, e.g. a thresholded GM-probability map (examples depicted in Fig. 13). If no mask were defined, i.e. the whole image is considered, gQED is almost equal to unconstrained Gaussian smoothing in voxel space.

When calculating the distance between two arbitrary voxels as the shortest path from one to the other, this path is now restrained by the mask. Speaking in analogs, traveling from one mountaintop to another requires hiking through the valley and the linear distance between the mountain tops is of little relevance.

The metric used for the distance is quasi-Euclidean, which is a necessity for calculation of geodesic distances. In two dimensions and without a mask, the quasi-Euclidean distance d_{qe} between two points P_1 and P_2 with coordinates (x_1, y_1) and (x_2, y_2) , respectively, is defined as

$$d_{qe} = |x_1 - x_2| + (\sqrt{2} - 1) \cdot |y_1 - y_2| \quad (14)$$

for

$$|x_1 - x_2| > |y_1 - y_2| \quad (15)$$

and

$$d_{qe} = (\sqrt{2} - 1) \cdot |x_1 - x_2| + |y_1 - y_2| \quad (16)$$

otherwise. In other words, while also generalizing this to masked 3D-images, the distance between two voxels is the shortest connecting path, where only voxels within the mask can be traversed and only crossed along one of their symmetry axes.

In contrast, the Euclidean distance d_e in two dimensions is defined as

$$d_e = \sqrt{(x_1 - x_2)^2 + (y_1 - y_2)^2} \quad (17)$$

For each of the n non-zero voxel in the mask, called seeds, the distances to all the other voxels may be calculated. In MATLAB this is implemented using the geodesic distance algorithm described in [25]. As the number of surrounding voxels scales with the distance to the power of three, the implementation of gQED considers only sub-volumes in the close vicinity of the seed, taking Gaussian smoothing into account:

For an intensity profile following a Gaussian function

$$g \propto e^{-\frac{d^2}{2\sigma^2}} \quad (18)$$

with standard deviation σ , the intensity at $d \geq 3.5 \sigma$ (≈ 1.5 FWHM) is well below 0.5 % of the initial intensity at $d = 0$. Therefore, contributions to voxels of greater absolute distance to the seed than 3.5σ may be considered insignificant.

Once the distances d of all significant voxels to seed i have been calculated, a Gaussian-weighted image g_i is computed as

$$g_i = I_i \cdot \frac{1}{(\sqrt{2\pi} \cdot \sigma)^3} e^{-\frac{d_i^2}{2\sigma^2}} \quad (19)$$

with the seed's intensity I_i . g_i describes only the smoothing of seed i 's signal to its neighbors, as if they had zero intensity of their own. Summation of all seeds' images returns the whole smoothed volume:

$$G = \sum_{i=1}^n g_i \quad (20)$$

It can be shown that summation of the seed images (for a non-masked volume and Euclidean metric) and a convolution are mathematically identical. In fact, it is merely an application of associativity and commutative properties. A Gaussian is a common choice for a smoothing kernel, for better comparability the method described above has also been implemented with the kernel used by SPM, as described in section 6.2.5 and Fig. 11. Data processed with SPM's kernel will be abbreviated as sQED or sED, depending on the metric used.

As an example, we use an arbitrary image vector u and kernel vector v (for simplicity both of length 5). With eq. (13) the convolution w of these two vectors is

$$w = \begin{pmatrix} \vdots \\ u_1 v_3 + u_2 v_2 + u_3 v_1 \\ u_1 v_4 + u_2 v_3 + u_3 v_2 + u_4 v_1 \\ u_1 v_5 + u_2 v_4 + u_3 v_3 + u_4 v_2 + u_5 v_1 \\ u_2 v_5 + u_3 v_4 + u_4 v_3 + u_5 v_2 \\ u_3 v_5 + u_4 v_4 + u_5 v_3 \\ \vdots \end{pmatrix} \quad (21)$$

gQED comes to the same results via the following steps:

$$w = \sum_i w_i = \begin{pmatrix} u_1 v_3 + u_2 v_2 + u_3 v_1 \\ u_1 v_4 + u_2 v_3 + u_3 v_2 + u_4 v_1 \\ u_1 v_5 + u_2 v_4 + u_3 v_3 + u_4 v_2 + u_5 v_1 \\ u_2 v_5 + u_3 v_4 + u_4 v_3 + u_5 v_2 \\ u_3 v_5 + u_4 v_4 + u_5 v_3 \end{pmatrix} \quad (22)$$

where

$$w_1 = u_1 \cdot \begin{pmatrix} v_3 \\ v_4 \\ v_5 \\ 0 \\ 0 \end{pmatrix}, w_2 = u_2 \cdot \begin{pmatrix} v_2 \\ v_3 \\ v_4 \\ v_5 \\ 0 \end{pmatrix}, w_3 = u_3 \cdot \begin{pmatrix} v_1 \\ v_2 \\ v_3 \\ v_4 \\ v_5 \end{pmatrix}, w_4 = u_4 \cdot \begin{pmatrix} 0 \\ v_1 \\ v_2 \\ v_3 \\ v_4 \end{pmatrix}, w_5 = u_5 \cdot \begin{pmatrix} 0 \\ 0 \\ v_1 \\ v_2 \\ v_3 \end{pmatrix}$$

To account for the different number of surrounding seeds contributing to each image voxel, where voxels close to the mask's surface obviously have fewer neighbors and thus express lower

intensity, the image may additionally be corrected by dividing each image voxel with the number m of its significant contributors:

$$G_{nc,i} = \frac{G_i}{m} \tag{23}$$

Since this scaling only influences absolute values of the voxels and not activation relative to their base level, there is virtually no change in the resulting activation patterns. Empirically, only changes in the second decimal place were observed.

6.2.4 Comparison in 1D

A numeric comparison of a “standard” 1D-convolution of a binary image with an exemplary inverse-distance kernel and the approach used for gQED is displayed in the table below where “...” denotes symmetric values in the vector. Only the central part of the convolution with the same size as the image is displayed.

Image	Kernel (0-padded)	Convolution	gQED (unmasked)
[0 0 0 1 1 1 0 0 0]	$\left[\frac{1}{5} \frac{1}{4} \frac{1}{3} \frac{1}{2} 1 \dots \right]$	$\frac{1}{60} [27 \ 47 \ 65 \ 110 \ 120 \dots]$	$\frac{1}{60} [27 \ 47 \ 65 \ 110 \ 120 \dots]$

Table 2 Smoothing of a 1D ‘image’

The term “zero-padding” describes that when image and kernel “slide across” each other, all values outside image and kernel are zero. For an image that has only continuous non-zero values, convolution and gQED-convolution return identical results, which is not surprising as they are mathematically the same. For the image vector in Table 2 there would also be no difference in the results between calculating the masked gQED-convolution (that is no smoothing across zeros) or using the convolution and subsequently masking the image.

However, the surplus value of the computationally slower gQED approach can be easily understood when the image contains non-continuous areas of non-zero values, which are treated as masked as in Table 3. For the following example only a single entry in the image vector has been changed to create two blocks of ones. The kernel used remained the same as in Table 2.

Image	Convolution	gQED (masked)
[0 1 0 1 1 1 0 0 0]	$\frac{1}{60} [57 \ 107 \ 95 \ 130 \ 135 \ 122 \ 65 \ 47 \ 27]$	$\frac{1}{60} [0 \ 60 \ 0 \ 110 \ 120 \ 110 \ 0 \ 0 \ 0]$
	Convolution (subsequently masked)	gQED (neighbor corrected)
	$\frac{1}{60} [0 \ 107 \ 0 \ 130 \ 135 \ 122 \ 0 \ 0 \ 0]$	$\frac{1}{60} [0 \ 60 \ 0 \ 55 \ 60 \ 55 \ 0 \ 0 \ 0]$

Table 3 Smoothing of a masked 1D ‘image’ with the same kernel previously used

For discontinuous areas a simple convolution and gQED may differ significantly, even when implicit masking is used, as offered in SPM. This issue is particularly present in the gray matter of the human brain with its high level of cortical folding. As previously explained, volumetric smoothing of signals which are spatially close but on different gyri may get mixed during smoothing and thus impede correct interpretation of activated areas.

The convolution implemented in MATLAB and SPM cannot properly handle masking or NaN (Not a Number) values. In SPM, NaNs are treated as zero during smoothing. If implicit masking is

specified as an option, NaNs are still treated as zero during smoothing and in a second step all voxels which were NaN before are then reset to NaN. Although this avoids mixture of different tissue types (e.g., gray and white matter) it may still smooth data across separate areas which are in spatial close proximity.

While a convolution of matrices including NaNs is possible using the function `nanconv` [26], the approach did not lead to the comparable results for the previously described test vector with zeros replaced with NaNs, as can be seen in Table 4 below:

Image	$[NaN\ 1\ NaN\ 1\ 1\ 1\ NaN\ NaN\ NaN]$
Kernel	$\begin{bmatrix} 1 & 1 & 1 & 1 \\ 5 & 4 & 3 & 2 \end{bmatrix}^1 \dots$
nanconv (default settings)	$\frac{1}{60} [137\ 167\ 187\ 202\ 214\ 202\ 187\ 167\ 137]$
nanconv ('edge')	$[1\ 1\ 1\ 1\ 1\ 1\ 1\ 1\ 1]$
nanconv ('nanout')	$\frac{1}{60} [NaN\ 167\ NaN\ 202\ 214\ 202\ NaN\ NaN\ NaN]$

Table 4 Smoothing of a masked 1D image using the `nanconv`-function

6.2.5 Comparison in 3D

In one dimension, distances between two vector elements are simply the absolute difference of the elements' indices. For two and three dimensions, a metric is to be used, where different metrics may lead to different distances between voxels. In Fig. 10 isosurfaces are displayed for four common metrics.

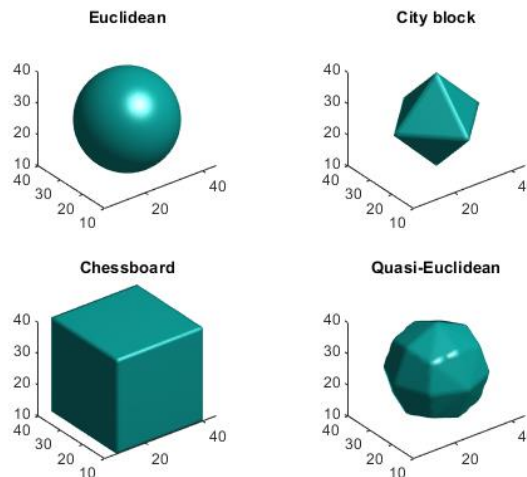


Fig. 10 Isosurface plots for distance transforms of a 3D-image; Image dimensions $[50\ 50\ 50]$; There is a single non-zero voxel at $[25\ 25\ 25]$; Each isosurface displays a distance of 15 units using the metric specified in the subplot's title. Image taken from MATLAB Documentation for function `bwdist()`.

Application of these different metrics and smoothing methods is given in Fig. 11. While smoothing an unmasked test image using the same mathematical procedure as implemented in gQED but with Euclidean metric and SPM's kernel (abbreviated sED below) nearly perfectly reproduced the SPM-smoothed image (differences were below 0.008 for a maximum intensity in the images of 100, see also Fig. 11), there are significant differences between smoothing with quasi-Euclidean metric in

combination with SPM's kernel (sQED) and SPM-smoothing of nearly 5.6 intensity units. The maximum difference between with a Gaussian Kernel and Euclidean metric to SPM's smoothing was below 2.1 and are assumed to be mainly attributed to differences in kernel width/steepness.

Smoothed images

Difference to SPM

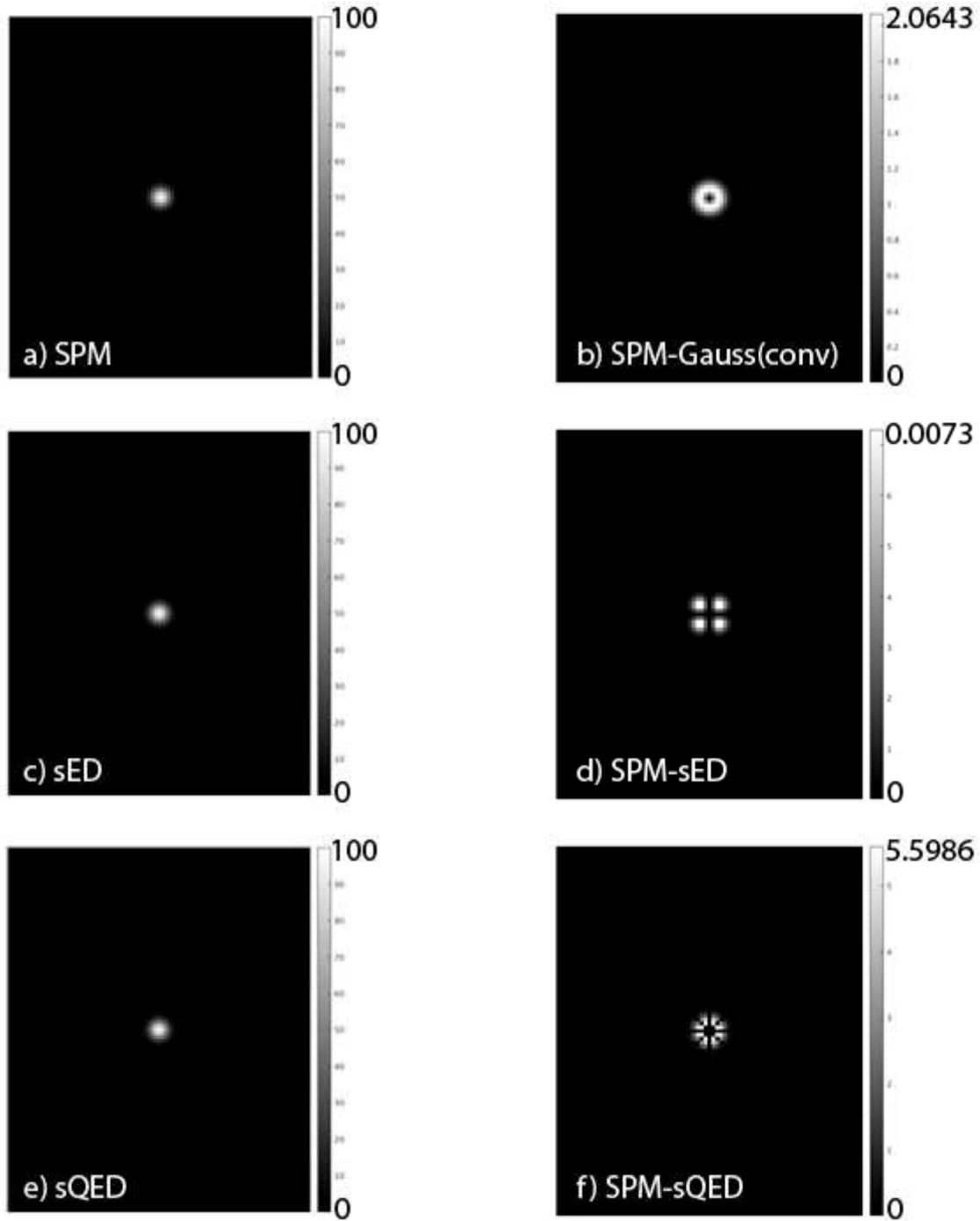


Fig. 11 Differences in voxel intensities for different smoothing approaches; left column: results of smoothing a single voxel of $I = 100$ with different kernels and metrics; right column: smoothed image obtained by various methods subtracted from SPM-result. Please note the different scaling of the right column.

In Fig. 11 f one can easily see that quasi-Euclidean and Euclidean metric are identical for the image's symmetry axes. The structure visible in Fig. 11d has been noted, but since its intensity is comparably low, its source was not identified.

It has to be stressed that the main conclusion from above observations is that gQED uses a correct implementation of a smoothing algorithm and produces similar results. The differences between the two metrics are not to be forgotten, but even if it were possible to use Euclidean metric for geodesic distances, unrestricted spatial smoothing and masked, geodesic smoothing still differ fundamentally. In the Results and Discussion section, the focus will thus be on differences in signal detectability, spatial distribution, and correct location of activated areas.

6.2.6 Adaptive Smoothing

Adaptive Weight Smoothing (AWS) – now also implemented as an SPM toolbox (aws4SPM) [27] - traces back to [28]. In 2000 Polzehl and Spokoiny first proposed locally constant smoothing with adaptive weights for point pairs in various image data, from satellite images to medical applications and also fMRI [29]. Their goal was to reduce over-smoothing of relevant discontinuities i.e. edges and borders of relevant structures such as buildings in satellite images or tissue boundaries in medical imaging, while at the same time removing noise therein. AWS' framework is dimensionality independent and requires no a priori assumptions such as anatomical information but detects borders within the (fMRI) images.

The iterative process of adaptive smoothing is reported to increase sensitivity, power and reducing the number of false positives [9] as well as being advantageous when used on higher-resolution fMRI data, which would often not be used due to its lower SNR and resulting difficulties in activation detection. [29]

In contrast to other smoothing methods, aws4spm requires already statistically processed data as input i.e. already defined and estimated contrasts. These are then used as a starting point for iterative, adaptive smoothing. Unfortunately, only statistical results and no smoothed 4D-image file is returned by the analysis stream, which is why this approach cannot be used for analysis in the time domain. Thus, only the spatial distribution of single subject data analyzed with aws4SPM will be presented in the Results section.

6.2.7 Surface Based Analysis – FreeSurfer/FS-FAST

The software and tool collection FreeSurfer roots in work by Fischl, Dale and Sereno ([30], [31] and [32]) and has evolved and been extended since then. Its roots and progress have been reviewed e.g. by Fischl in [33].

FreeSurfer's most prominent features are the segmentation of anatomical scans and subsequent construction of a surface model of the cortex in a spherical coordinate system as proposed in [32]. Since FreeSurfer uses the white matter surface instead of GM for registration it is independent of GM atrophy. While useful during analysis a spherical activation map would be hard to interpret. Therefore, results are commonly displayed on a slightly inflated brain as depicted in Fig. 12.

This surface-based approach reduces anatomical variance in the location of corresponding sulci and gyri and thus may theoretically reduce the number of subjects needed for statistically analysis as suggested in [34]. The spherical model can not only be used to compare anatomical features between subjects such as cortical thickness, but also as a starting point of surface based functional analysis as implemented in FS-FAST (FreeSurfer Functional Analysis Stream).

Smoothing on the surface is achieved by weighted means of the BOLD-intensities that have been mapped to the surface model during coregistration of anatomical and functional scans (i.e. nodes on the surface have been assigned BOLD values). As brain ‘inflation’ removes gyration, data points which have been spatially close but anatomically distant before are now also spatially (on the inflated surface) distant with many vertices between them. This has been visualized by adding two colored points on the brain surface representation in Fig. 12. With volumetric smoothing (gyrated brain on the left) the signals at the location of the two points which are partially buried in the sulcus would mix. If only one of these regions were activated, still both would be detected as activated after smoothing or rather a continuous active region would be seen stretching from one point to the other. Smoothing along the vertices on the surface model would mix the signals to a much lower extent as on the surface model they are further apart (in the schematic cross section depicted below the distance roughly doubled due to inflation).

For additional comparison between purely volumetric smoothing and gQED-smoothing the data has also been analyzed with FS-FAST. According results will be presented in section 7.2.2.

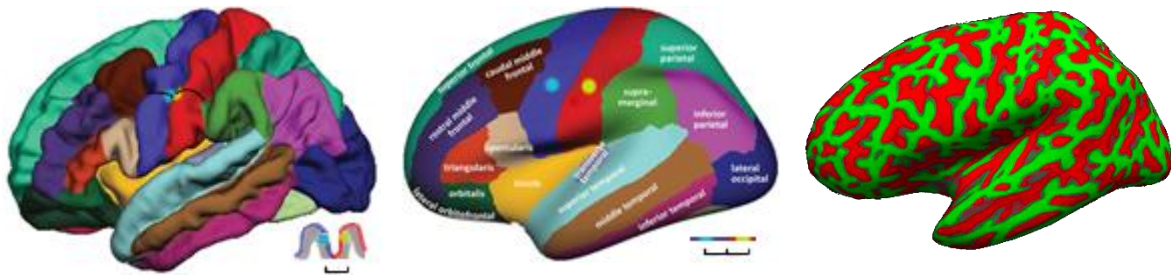


*Fig. 12 Inflated surface representation of the human brain; **Left and center:** color-coded template brain prior and post inflation, sagittal cross section of pre- and postcentral gyrus depicted below; Adapted from [35] **Right:** Color coded gyri and sulci on inflated brain; Adapted from andysbrainbook.readthedocs.io*

6.3 Experimental Data

While processing artificial data is a good test for basic functionality of gQED, it would not only take highly sophisticated models to achieve truly realistic datasets, but the desired field of application still would be real functional data. Therefore, the different algorithms were tested on an experimental fMRI data set from a clinical study.

6.3.1 Population

Imaging data (anatomical and fMRI images) were generously provided by the Neuroimaging Labs, Department of Psychiatry and Psychotherapy, Medical University of Vienna and had been acquired in a previously completed and thematically unrelated pilot-study on task duration in fMRI vs fPET [36] on 21 healthy subjects. The study was approved by the ethics committee of the Medical University of Vienna (ethics number: 1479/2015) and all subjects had given written informed consent. 20 of the recruited 21 subjects were included in the analysis of [36]. One subject was excluded due to excessive head movement during measurement. For reasons explained below, two more subjects were excluded in the analysis for this thesis, reducing the total number of subjects to 18 (9 male, mean age \pm sd = 26.2 \pm 4.3 years).

6.3.2 Measurement

Images had been acquired using a hybrid PET/MRI scanner (Siemens mMR Biograph; anatomical scan: magnetization prepared rapid gradient echo sequence (MP-RAGE), TE/TR 4.2/2200 ms, voxel size $1 \times 1 \times 1.1 \text{ mm}^3$); fMRI: EPI (echo-planar imaging), TE/TR 30/2000 ms, voxel size $2.5 \times 2.5 \times 3.3 \text{ mm}^3$). During measurement, four 30-second blocks of two uncorrelated tasks were simultaneously performed: Observation of landscape video clips while repeatedly tapping the right thumb³ to each finger of the right hand (sequence: index to small finger) at about 1 sequence per second. Breaks between tasks lasted 15 seconds. Design matrices as well as log files were provided for further analysis steps.

The tasks are expected to evoke major activation in the visual cortex (landscape video observation) and the left motor cortex (since the right hand is used) with possible activation in the supplementary motor area. For this thesis, the main focus was on the motor cortex signal as it is localized near the central gyrus and separation and correct allocation of pre- and postcentral signal is a challenging task which could especially benefit from methods such as gQED.

6.3.3 Volumetric Analysis

For gQED and ‘standard’ spatial smoothing a SPM12-preprocessing pipeline had been used, consisting of slice-time-correction (middle slice as reference), realignment (register to mean, quality = 1), coregistration to anatomical images and spatial normalization to MNI-space (Montreal Neurological Institute).

6.3.3.1 Normalization

As explained in section 5.2.5, normalization does usually not result in perfect matches of the whole brain. While overlapping cortices would be generally of great interest for statistical analyses, it is especially important when masks are applied to a group of subjects, as implicitly done when using gQED smoothing.

As a more sophisticated and already established normalization approach CVS [8] was put to the test. CVS is part of the FreeSurfer environment, thus makes use of not only the overall brain anatomy but also the brain’s gyration when calculating a morph from subject to template brain. This morph was then applied to the ST-corrected, realigned and coregistered fMRI data. Further processing (smoothing) and statistical analysis was then performed in the same way as on other volumetric data sets.

6.3.3.2 Masking

Masking of functional data prior to smoothing may serve several purposes such as exclusion of areas which are not of interest and assumed to increase noise and reduce activation detectability in nearby structures. Masked voxels though may not be completely excluded during smoothing as it is the case in SPM where they are regarded as zero-valued during convolution. Thus, even smoothing with masks may transfer signals across areas in close proximity which may then affect activation maps in so called ‘crosstalk’ and reduce specificity in activation. When inherently no crosstalk is introduced during smoothing (as it can be the case for well-masked gQED-smoothed data and in

³ Due to difficulties in canalization needed for fPET two subjects used their left hand instead of their right hand, which caused activation in the opposite motor cortex. They still were included in the original study, though, by mirroring their data along the sagittal plane. Although considered at first, these two subjects were eventually excluded from the analysis for this thesis work as simply flipping activation does not consider anatomical differences between right and left hemisphere.

surface-based analysis) still some false-positive activity may be detected, though. This can be attributed to low image resolution, spatial extent of the BOLD-response and/or faulty signal projection during brain inflation in surface-based analysis.

A crucial factor in gQED-application is the choice of a mask. Due to their widespread availability, tissue probability maps (TPM) included in SPM have been used along with the MNI152 template. A liberally thresholded mask, i.e. a large mask including voxels of already low GM- and high WM- and/or CSF probability, does not replicate gyri and sulci well but is unlikely to cut away relevant voxels. One benefit of smoothing with gQED, though, lies in its ability to smooth within the GM and not mixing geodetically far apart activations, such as activations on either side of a sulcus, as well as signal from different tissues. Within a liberal mask, though, there is no distinction between functional/geodesic and Euclidean distance, that is leaving the different metrics used aside.

Too conservative masks on the other hand, which use high GM-probability thresholds, may exclude neural activation of interest due to either i) remaining anatomical variability between subjects after normalization, that is subject gyri do not match template gyri, or ii) activation closely located to the GM-border, where the GM-TPM exhibits lower values.

Therefore, during data analysis a range of thresholds has been used. A much more time-consuming approach following brain anatomy even closer would be to segment each subject's GM and use individual masks (with individual geodesic distances) for first level, i.e. intra-subject-analysis. This impedes group level analysis, though, as anatomical differences are not taken care of and the degree of smoothing in the same location for different subjects may differ.

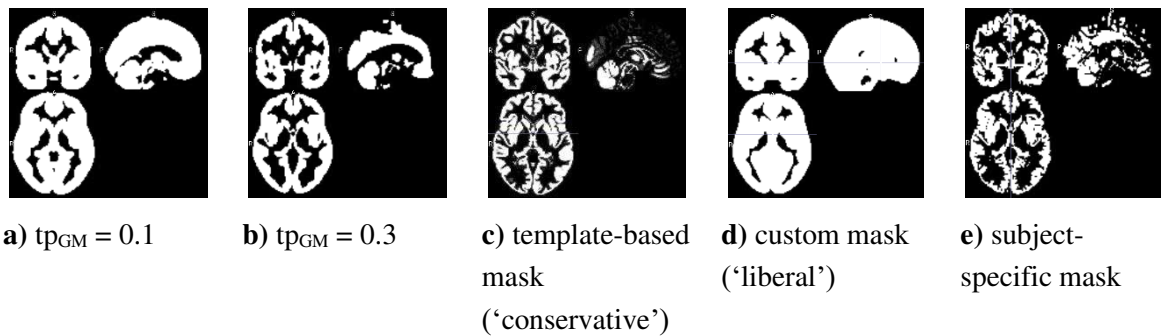


Fig. 13 Multi-planar views: Coronal, sagittal and axial slices of several gray matter probability-maps; a & b: Exemplary selection of thresholds tp and the resulting GM-mask of a TPM; c: MNI152 template-derived GM mask; d: custom mask derived by combining several tissue thresholds ('Fullbrain' - $tp_{WM} > 0.9$); e: GM-segmentation derived from a single subject's anatomical scan

6.3.4 Surface-Based Analysis

Analysis in FreeSurfer/FS-FAST followed a standard procedure consisting of processing anatomical scans (skull stripping, surface reconstruction) and functional images. Functional processing involves in order of execution: template creation, mask creation, intensity normalization, registration to anatomical data, motion correction, slice-time correction, spatial normalization, and resampling to common space and smoothing. (Note that FreeSurfer applies motion correction first instead of ST-correction.)

In FreeSurfer three common subspaces are used: both cortical hemispheres, each in surface space, and subcortical structures in volume space. Smoothing and analysis is performed in the respective spaces. Afterwards, single subject analysis and group analysis is performed for each subspace, followed by multiple comparison correction. Subcortical results will not be presented here due to lacking relevance for this thesis.

6.3.5 Statistics

On subject-level, for each dataset all voxels' BOLD time-courses were tested for significance with respect to the experimental finger tapping task tapping task (block-design, see figures 2 and 9). The expected time course for brain regions involved in the task is derived from convolution of the HRF with the binary design-vector where zeros stand for 'rest' and ones for 'task'. SPM and FreeSurfer create this vector from onsets and task durations specified in seconds or frames. The time course of task and BOLD signal are similar to the one depicted in Fig. 2.

Further regressors involved motion parameters derived during realignment to exclude any signal variation caused by head motion.

All reported T-values are corrected for multiple comparisons. For volumetric smoothing methods (SPM, aws4SPM, gQED) FWE (family-wise error) correction on voxel level with $p < 0.05$ was used. For FreeSurfer analyses multiple comparison correction was performed with 5000 permutations and voxel-wise threshold $vwthresh$ of

$$vwthresh = 1.3 = -\log_{10} p, \quad p = 0.05 \quad (24)$$

FWHM of all results reported was 8mm. In aws4SPM FWHM cannot be set explicitly but via bandwidth

$$h_{max} = 0.43 \cdot FWHM \quad (25)$$

as explained in [37].

7 Results

7.1 Artificial Data

7.1.1 Single Subject

The influence of different smoothing methods applied to single-subject artificial data was analyzed in time (see Fig. 14) as well as in space (Fig. 15) since both play an important role in accurate activation detection and localization and thus functional analysis.

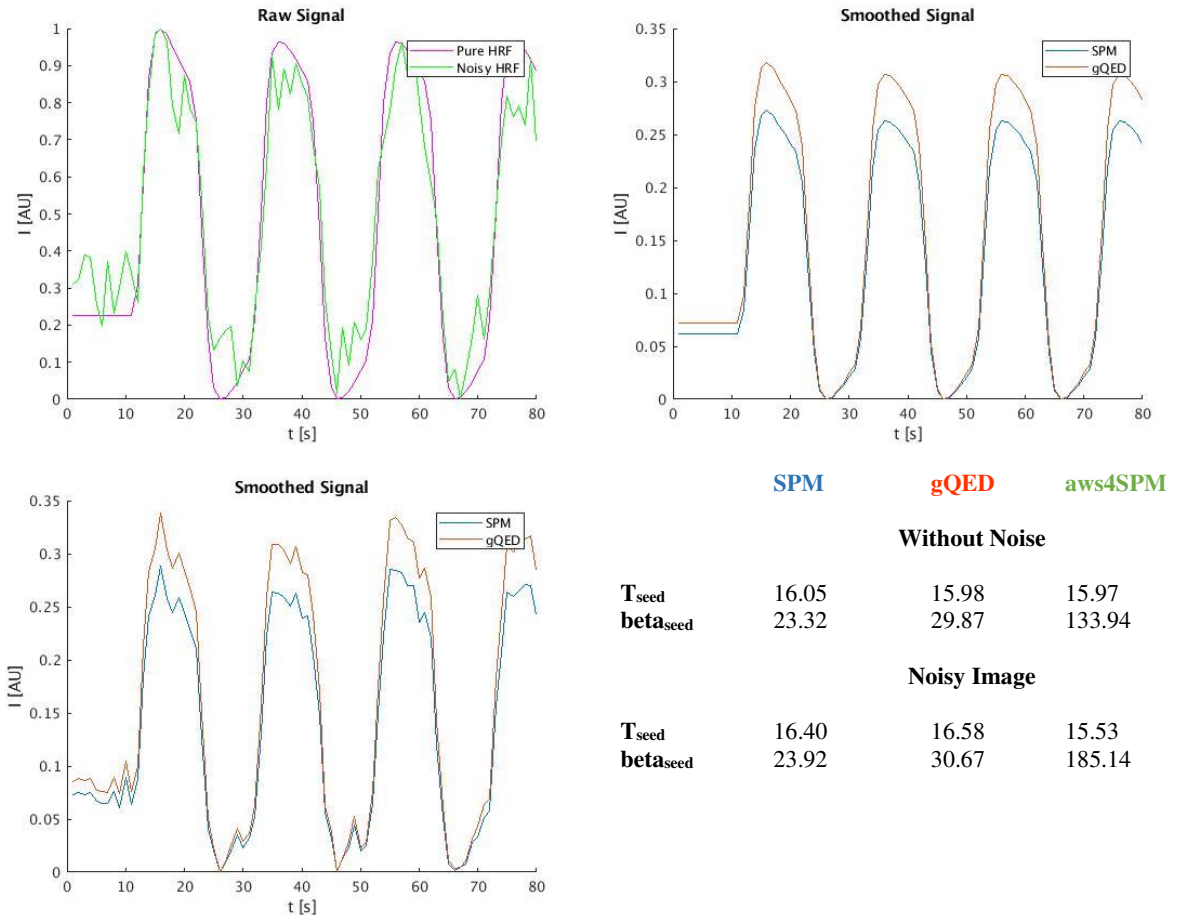


Fig. 14 Artificial BOLD-signal time courses ; **Top left:** Signal with and without added noise; **Top right:** Non-noisy signal post smoothing (SPM and gQED, no time course returned by aws4SPM-procedure); **Lower left:** Smoothed noisy signal; **Lower right:** Statistics for seed voxels. Remark: Due to large noise components and resulting signal variability the seed did not always exhibit the largest T-value.

For data presented in this section a GM-segmented and thresholded MNI152-template served as the cortex in which the signal occurred. For SPM and gQED (implicit) masking was used i.e. voxels outside of the cortex were excluded (gQED) or set to zero during smoothing and reset to zero/NaN afterwards (SPM). This approach using heavily masked data makes differences between SPM relying on Euclidean distances and gQED more visible.

Especially for non-noisy signals the difference between purely volumetric/Euclidean smoothing (SPM) and the other methods is well visible: Even with the mask used, the activation pattern derived with SPM resembles approximately a sphere and is in stark contrast to how the signal spreads within the brain. Both gQED and aws4SPM show much smaller activation patterns that follow the underlying anatomy more closely.

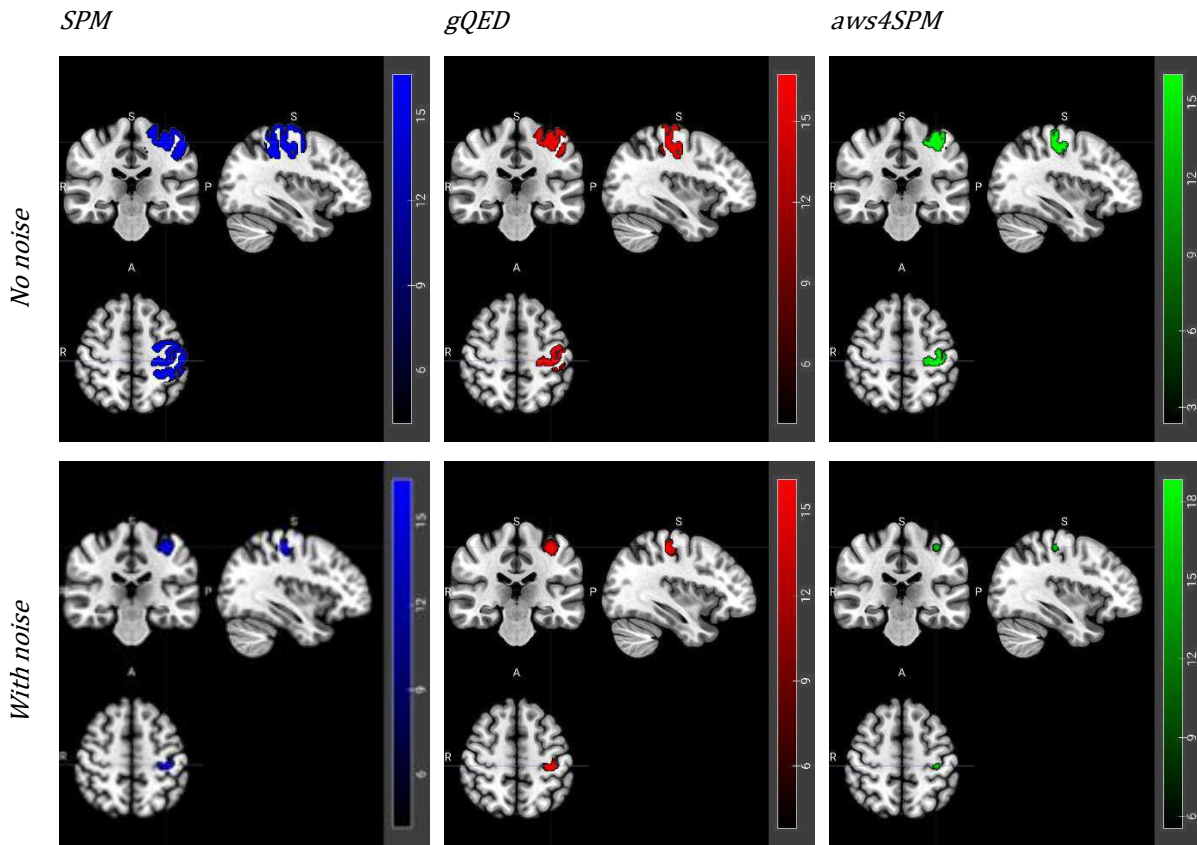


Fig. 15 Statistically relevant activation patterns (thresholded T -statistics) for different smoothing methods (left to right: SPM, gQED, aws4SPM) of an artificial BOLD-signal. **Top row:** T -statistics for non-noisy data (time course as in Fig. 14 top right); **Bottom row:** T -statistics for noisy data (time course as in Fig. 14 bottom left)

On a single-subject basis smoothing serves little other purposes than increasing SNR as of course no differences in anatomy and/or uncertainties in normalization need to be compensated for. To analyze the influence of different smoothing methods on temporal SNR (tSNR) 20 artificial data sets were created. The used GM map in which the signal propagated as well as the seed location and signals' time course (i.e. the underlying design matrix) were identical. Random noise was added to each data set. As can be seen in Fig. 16 mean tSNR for the seed voxel increased with both smoothing methods (gQED and SPM).

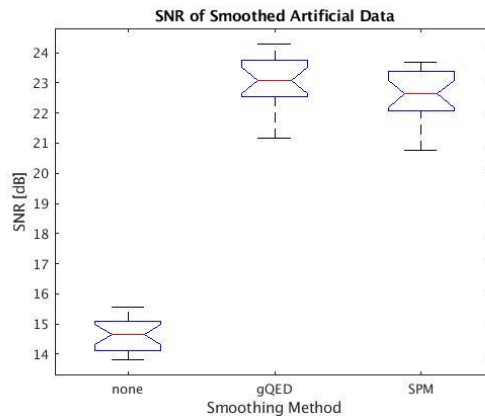


Fig. 16 Boxplot of the SNR of 20 artificial subjects prior to and post smoothing

7.1.2 Group Statistics

7.1.2.1 Artificial Data on MNI GM Mask with Identical Seed Location

As a second step in performance analysis of smoothing approaches, a simulated study (a set of 20 artificial measurements) was created using a more complex model but still with identical brain anatomy and seed location as described in section 6.1.

Main results of the group analysis are presented below in Table 5. No spatial variation of the maximum T-value and only little variation in the statistic's magnitude was observed.

	Liberal mask		Conservative mask	
	SPM	gQED	SPM	gQED
T_{max}^{brain}	9.08	9.31	9.12	9.33
$[x, y, z]$	[-36, -26, 54]	[-36, -26, 54]	[-36, -26, 54]	[-36, -26, 54]
T_{thresh}	7.34	7.44	7.13	7.25

Table 5 Resulting activation clusters and corresponding statistics for a simulated study with identical brain template and identical seed for all 'subjects'

7.1.2.2 Artificial Data on Real Subjects' GM Masks

Third in artificial data analysis another simulated study was created using the more complex model, this time also varying brain shape and thus also the seeds' location. Results can be found below in Table 6.

This model was only smoothed with a liberal group mask, as subject-specific masks would not allow for meaningful group-statistics and a more restrictive mask would hardly fit all subjects without excluding certain anatomical areas in certain subjects. This issue is further addressed in sections 5.2.4, 6.3.3.1, 7.2.2 and 8.1.

	Liberal mask	
	SPM	gQED
T_{max}^{brain}	16.45	16.41
$[x, y, z]$	[-34, -22, 50]	[-34, -22, 50]
T_{thresh}	7.24	7.45

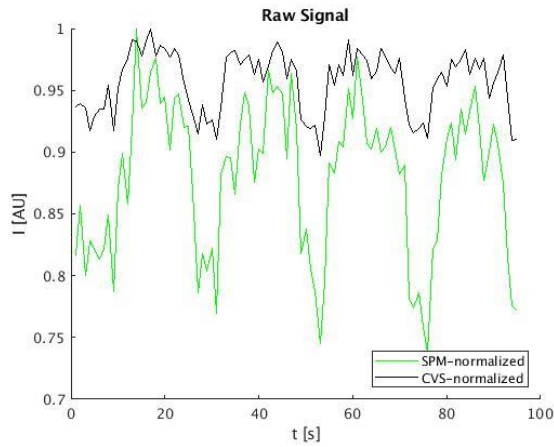
Table 6 Resulting activation clusters (only global maximum reported) and corresponding statistics for a simulated study with different brain template for all 'subjects'; Brain templates were derived from normalized, segmented anatomical scans of real subjects

7.2 Volumetric Experimental Data

7.2.1 Single Subject

For the following considerations, a single representative subject was chosen. Similar to the analysis of artificial data the time courses (Fig. 17) and spatial extent of activation patterns were of interest. As aws4SPM did not return smoothed 4D data and thus no time courses but merely the resulting statistics and activation maps, aws4SPM results are shown in Fig. 18 displaying activation maps only.

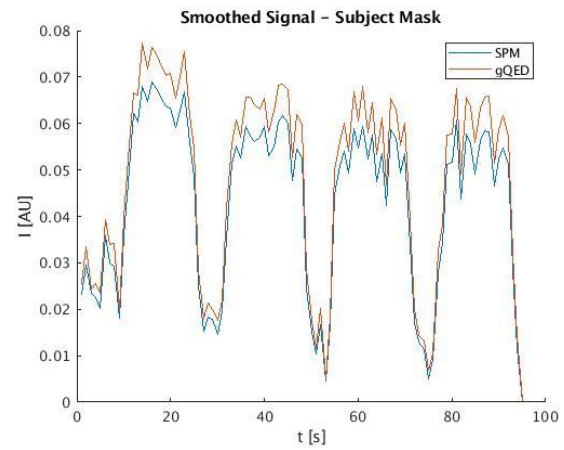
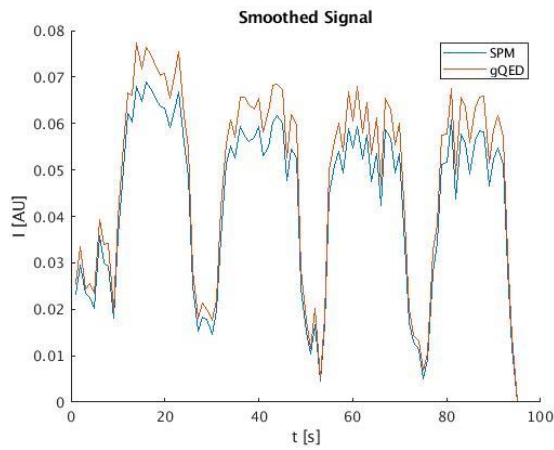
Surface-based Smoothing of Brain Imaging Data in Voxel Space



Anat. Norm.	Mask	SNR_{SPM}	SNR_{gQED}
SPM	Group	43.97 dB	42.93 dB
[-42, -26, 44]	Subject	41.68 dB	40.18 dB
CVS	Group	41.50 dB	40.09 dB
[-42, -10, 62]	Template	39.25 dB	37.85 dB

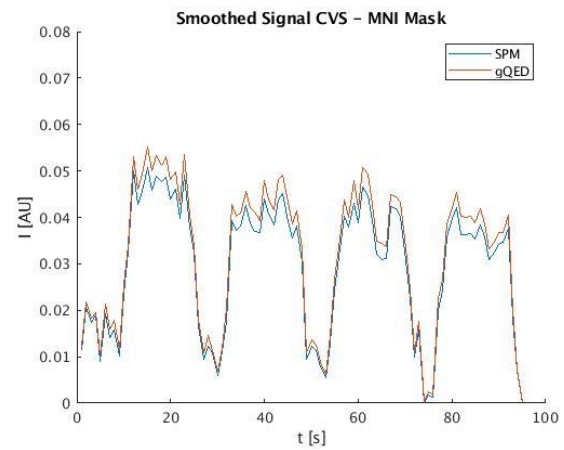
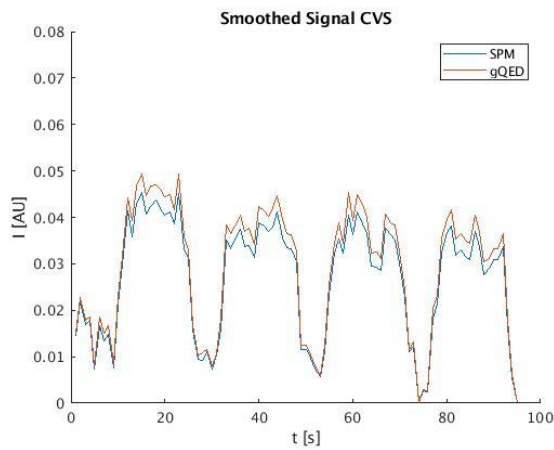
a) Scaled time course (max = 1) of spatially normalized but unsmoothed data

b) $tSNR$: Signal: $Y = \tilde{X} \cdot \beta$ Noise: ϵ



c) Time course of smoothed data (group mask)

d) Smoothed data (subject-specific mask)



e) CVS-normalized, liberally masked, smoothed data

f) CVS-normalized and restrictively masked, smoothed data

Fig. 17 Single-voxel time courses of a representative subject; The chosen voxel had the highest T-statistic in this subject's statistical analysis for either normalization method

The reader may have noticed that normalization procedures heavily influence signal smoothness and the range of the changes in BOLD-signal as compared to its maximum value. The different smoothing procedures additionally influence the magnitude of the activation's time course. Both, a

rather smooth signal but with still large differences between task and no-task condition would be desired. This of course is not easily possible as smoothing is some sort of averaging and averaging active with non-active voxels will inherently result in less visible effects. With more conservative masking the averaging effect is reduced, which is why the signals are larger in the right column.

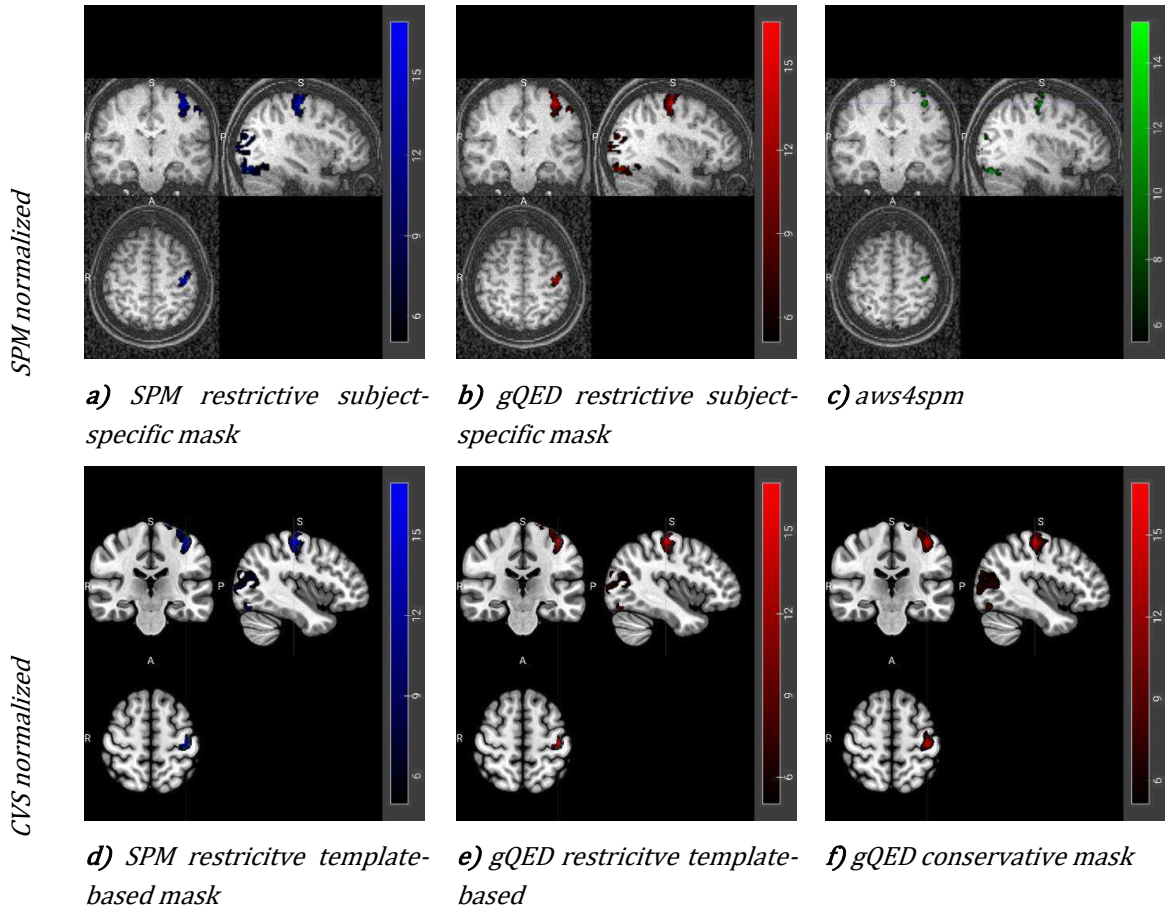


Fig. 18 Single-subject activation maps (T-statistics) with different normalization and smoothing approaches

Single-subject activations were analyzed using boxplots (Fig. 19) as changes therein may affect group statistics relying on the subjects' effect strength files as input. Maximum values for T-statistics and effect strength (beta) were automatically extracted for each subject from a cube surrounding the motor cortex.

It can be observed that the effect strength (beta) derived with gQED is larger than with SPM-smoothing, while T-contrasts stay nearly the same, especially when compared on within-subject level.

SPM normalization – group mask

CVS normalization – restrictive mask

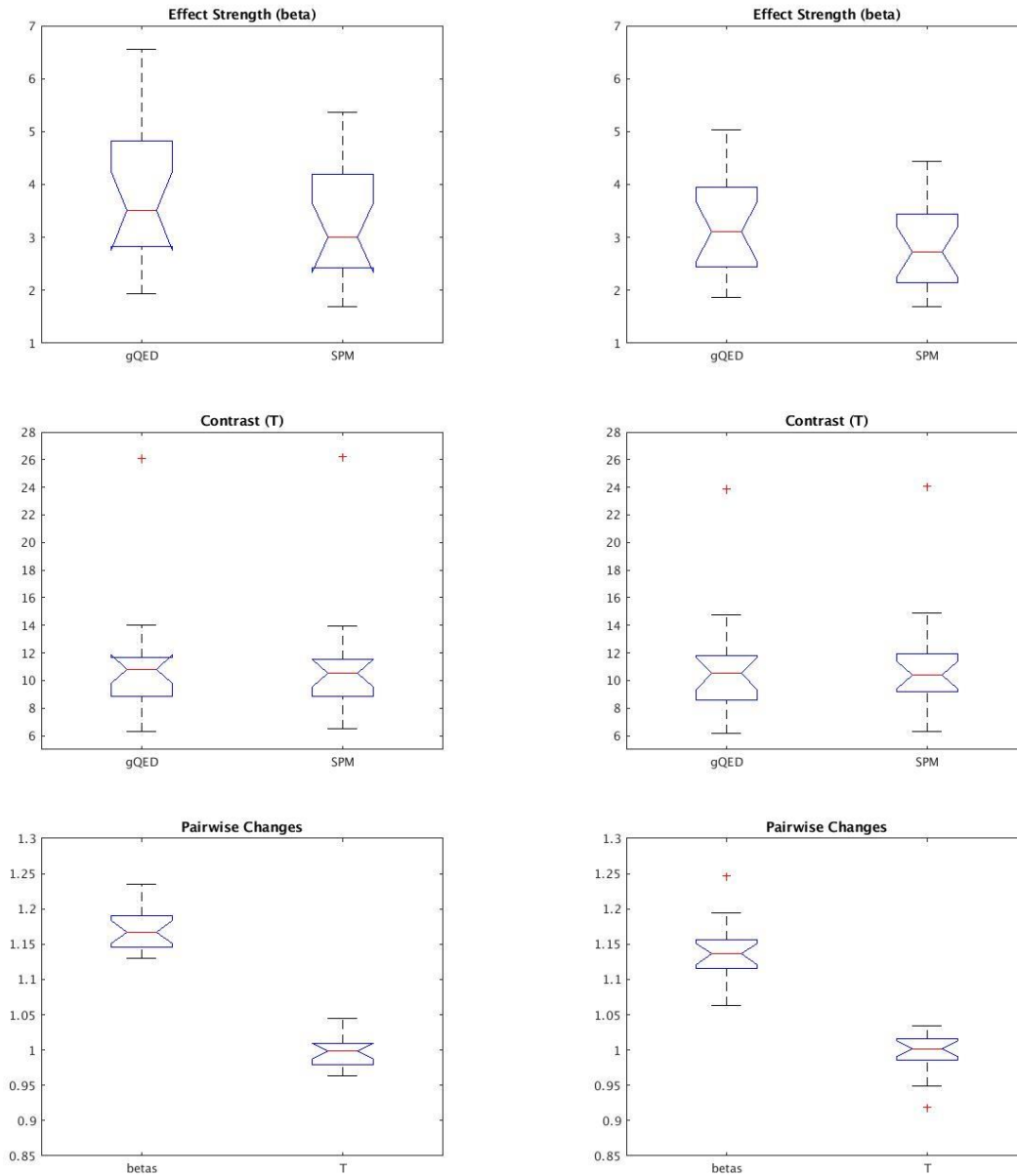


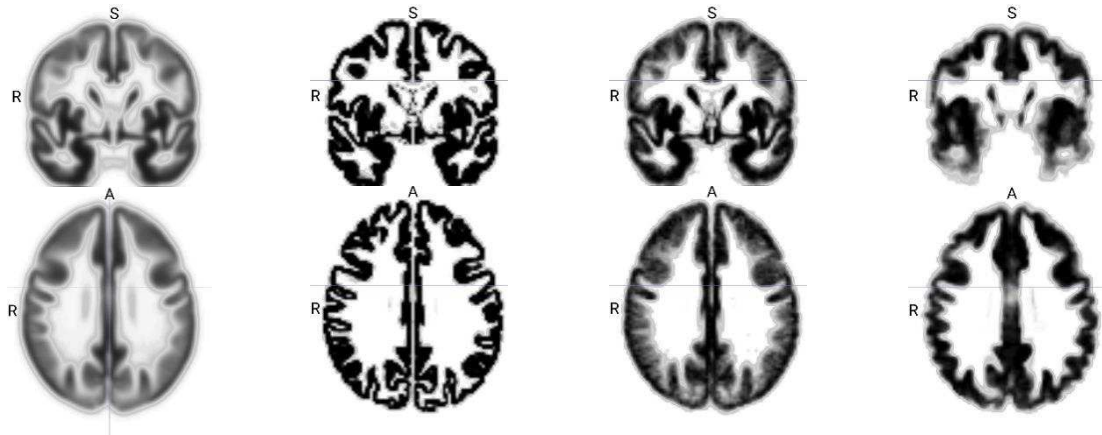
Fig. 19 Boxplots visualizing the (pairwise) differences in magnitude of single-subject effect strength (first row) and *T*-statistics (second row). **Left** column: SPM-normalized data smoothed with a liberal mask; **Right** column: CVS-normalized data smoothed with a restrictive mask. Pairwise Changes visualize fractions of each subject's values derived with gQED divided by SPM-smoothed results

7.2.2 Spatial Normalization

The importance of spatial normalization and the necessity of achieving good anatomical overlap between subjects has been stressed previously.

As a measure for normalization quality the normalized data was segmented, and group-averaged tissue-probability maps were created as displayed in Fig. 20 c) and d). TPMs were then visually compared by means of local tissue probability (darker color represents higher probability and overlap) and spatial extent and visibility of anatomical structures therein.

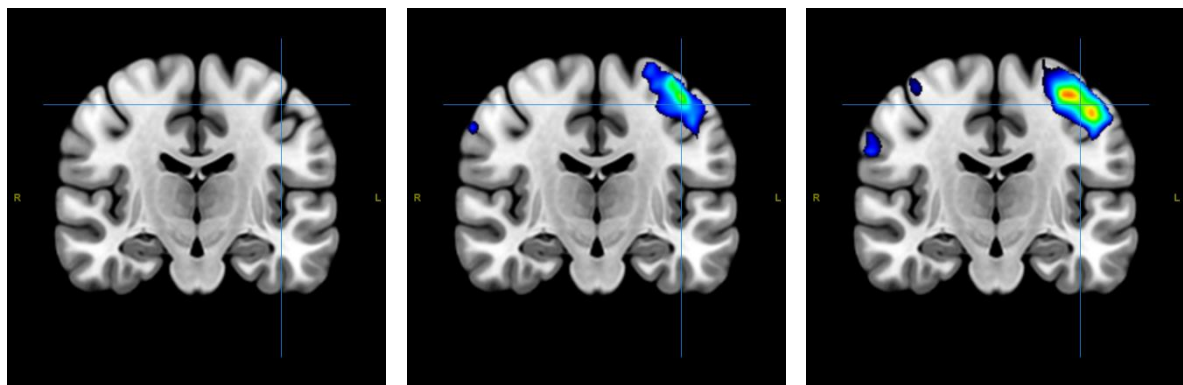
As can be seen in Fig. 20 below, the group-averaged tissue-probability maps for gray matter derived with CVS are similar to the GM-TPM of a segmented template brain indicating good normalization, whereas SPM-normalization barely exhibited well defined gyri and sulci.



a) Gray matter TPM **b)** GM-segmented MNI152 template **c)** SPM-normalization TPM **d)** CVS-normalization TPM

Fig. 20 Gray matter probability maps : a) TPM as distributed with SPM b) GM map created by segmentation of the MNI152-template using SPM c) scaled sum of subjects' GM maps when normalized with SPM d) scaled sum of subjects' GM maps when normalized with CVS

Additionally, group activation maps were used as shown in Fig. 21. Based on the assumption that the finger-tapping task in the experiment evokes relatively well defined and constrained brain activity in the subjects, it was concluded that for increasing normalization quality T_{max} should increase, activation cluster size should decrease and show more inherent structure. Local extrema and shape of activation patterns should additionally correspond better to the template brain anatomy. Corresponding statistics can be found in section 7.2.4.



a) Anatomical brain template **b)** Statistics derived from SPM-normalized data **c)** Statistics derived from CVS-normalized data

Fig. 21 Spatial differences in statistical maps derived from differently normalized data; For better visualization the same color maps were used ranging from respective T_{thresh} to T_{max} for each data set;

In Fig. 21 above statistical maps derived with SPM- and CVS-normalization and identical smoothing procedures are shown overlaid on an anatomical template slice. CVS-normalization

shows two well-pronounced local maxima within the cluster corresponding to the finger-tapping-task. Additionally, these agree better with brain anatomy than SPM-normalized data.

Lastly, even with much more restrictive masks the T-values and location of maxima should change little with good normalization. Results supporting these claim and in favor of CVS-normalization are shown in section 7.2.4.

7.2.3 Masking

The purposes of masking have been explained previously in section 6.3.3.2. In Fig. 22 group level statistical maps are presented on the same CVS-normalized data but with two different masks (see Fig. 13 c) and d)) and two smoothing methods for restrictively masked data. Although masking can of course influence resulting statistics the aim here is to show the spatial extent and inherent structure (local maxima) of areas detected as active. Therefore, no color bars are shown here.

Two major differences between the images are easily detected: First, in the left image there is no activity visible in the right postcentral gyrus (i.e. in the left part of the image). This is partially caused by the visualization, though: This cluster was still detected but with its most superior extent slightly inferior as compared to other methods, making it just not visible in the slice shown. The other major difference is the visibility of activation in the right supplementary motor area for both SPM-derived images but not gQED.

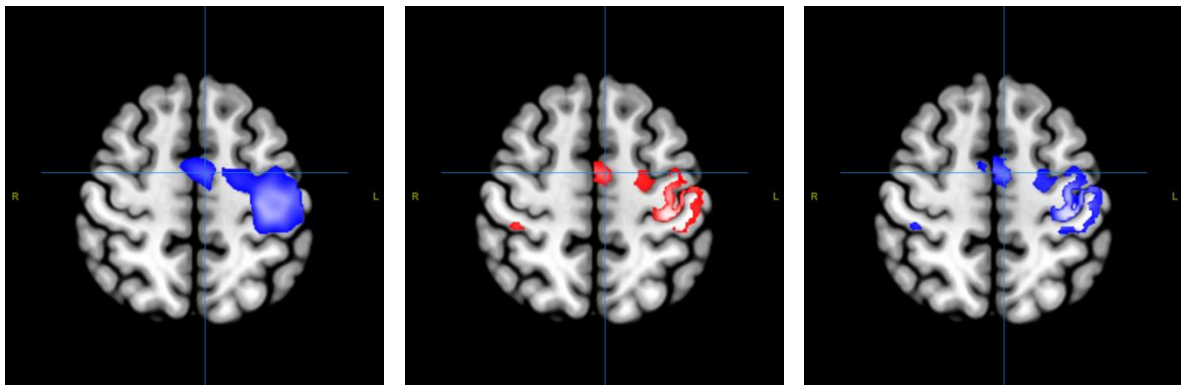


Fig. 22 Group statistics (T) of CVS-normalized data; Left to right: SPM smoothing with liberal mask, gQED smoothing in restrictive (conservative) mask, SPM-smoothing with restrictive mask;

7.2.4 Group Statistics

The results of volumetric group analysis for experimental data are presented in Table 7 and Fig. 23 for either volumetric normalization method and smoothing method. For CVS-normalized data two masks were used. SPM-normalized data was deemed to contain too large inter-subject anatomical variability to use a restrictive mask (see Fig. 20).

	SPM-normalization		CVS-normalization			
	Liberal mask		Liberal mask		Conservative mask	
	SPM	gQED	SPM	gQED	SPM	gQED
T_{max}^{motor}	16.36	16.91	19.11	18.34	16.54	16.07
$[x, y, z]_{max}^{motor}$	[-42, -26, 44]	[-42, -26, 44]	[-42, -10, 62]	[-42, -10, 62]	[-42, -10, 62]	[-42, -10, 62]
T_{thresh}	7.51	7.73	7.13	7.35	6.83	6.98

Table 7 Statistics derived with different masks, normalization and smoothing procedures

The enormous influence the tested normalization procedures have on resulting group statistics is well visible in Table 7: Large difference between T statistics for the same smoothing method and same mask but different normalization algorithm can be observed. Additionally, the T-levels for the restrictive mask and CVS-normalization are similar in magnitude to the ones with SPM-normalization, which included a much larger volume which means that there is little risk of excluding relevant voxels.

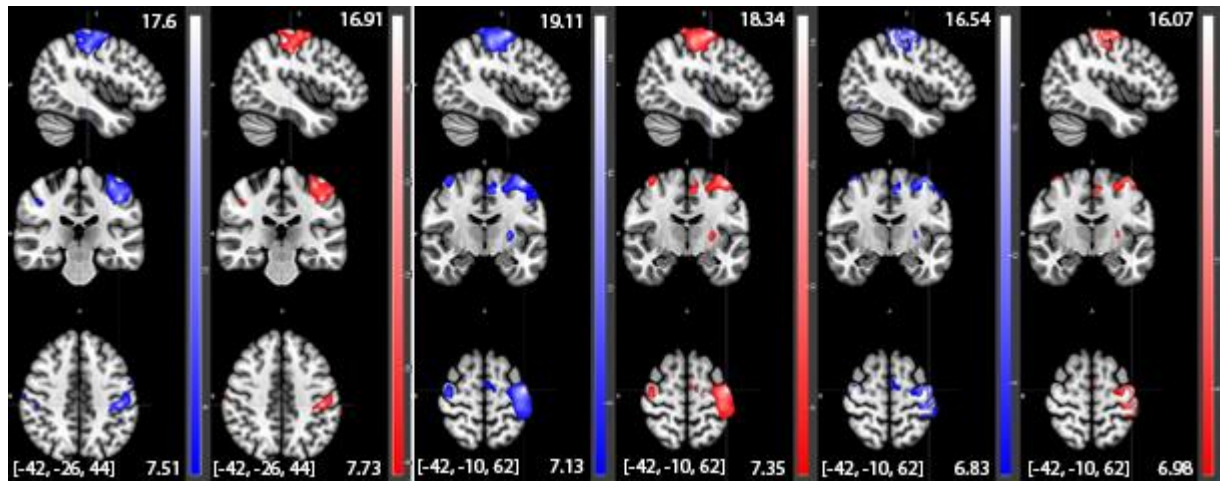


Fig. 23 Activation patterns derived from different smoothing methods; Order (left to right) is the same as in Table 7 above; The coordinates show the motor cortex' maximum of activation which differ between the two normalization procedures used. Please note the differently scaled color bars which are necessary since threshold and maximum T-values varied

7.3 Surface-Based Experimental Data

Data from surface-based analyses on subject- and group-level are presented below. As the left primary motor cortex was of interest only in this thesis work and FreeSurfer calculates and visualizes statistics separately for each hemisphere, solely the left hemisphere is shown and only from the most relevant angle (that is the median surface is not shown).

7.3.1 Single Subject

Results are shown for the same representative subject as before. Major activation clusters are visible in the post-central gyrus, only slightly expanding towards the pre-central gyrus, and in the visual cortex (as the experimental task combined finger-tapping with watching of videos). Few small additional clusters, some also exhibiting deactivation (blue) are visible. Please note that deactivation could also be detected in volumetric analyses but was not visualized.

For easier comparison between the two different visual representations of the brain volumetric results have also been mapped to the FreeSurfer template.

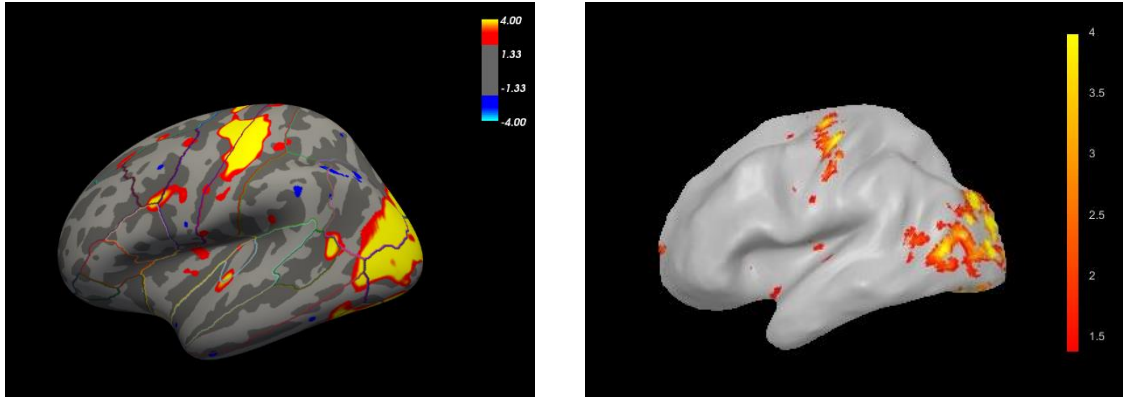


Fig. 24 Single subject's contrasts calculated with FS-FAST and visualized in FreeView (**left**) and a projection using mni2fs MATLAB toolbox of contrasts calculated in voxel space (gQED, subject-specific mask) on the inflated brain template (**right**). Colors and color bars show 'significances' as $-\log(p)$

7.3.2 Group Statistics

Group statistics derived with FreeSurfer/FS-FAST are shown and visualized below. The surface-visualization makes difference between (surface-) single-subject-level and (surface-)group-level easily visible: the visual cortex signal is more refined, in contrast to the motor cortex, e.g. there is much more activation in the pre-central cortex than for the single subject shown before. Activation is shown prior and post multiple-comparison correction.

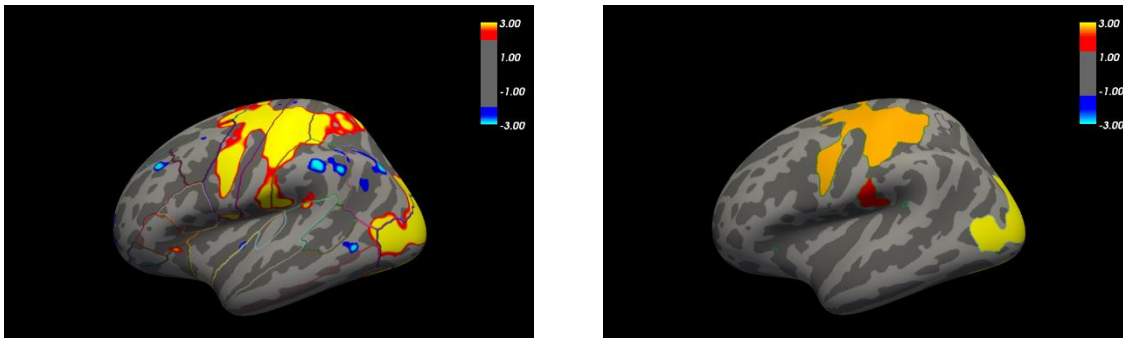


Fig. 25 FreeView visualizations of group-statistics calculated with FS-FAST; Colors and color bars show 'significances' as $-\log(p)$; **Left**: Data prior to multiple comparison correction; **Right**: Clusters after multiple comparison correction using random permutations.

After multiple-comparison correction FreeSurfer outputs a summary file whose content is shown below, and which allows for some – though limited – comparison with volumetric results by stating corresponding volumetric (MNI-)coordinates of the cluster maximum. The limited comparability is mainly rooted in the spatial shifts of single-subject activation due to the normalization procedure.

Cluster No	T_{\max}	Size (mm ²)	MNI-Coordinates	Annotation
1	13.073	8046.57	[-15.7, -89.7, -7.2]	Lateraloccipital
2	11.316	4443.33	[-39.2, -29.1, 58.1]	Postcentral (motor area L)
4	5.073	423.05	[-45.1, -26.6, 22.0]	Supramarginal

Table 8 Results excerpt of FS-FAST second level analysis for the left hemisphere; Font colors match the clusters as depicted in Fig. 25 right.

8 Discussion

In the course of this thesis work it became apparent that advanced smoothing methods can barely be analyzed independently and without taking previous preprocessing steps and especially spatial normalization into account. The reader shall thus be reminded, that in the following discussion – even if not always explicitly stated – observations are made on processes and metrics which directly and indirectly influence the performance of smoothing algorithms in general and the smoothing procedures described herein.

Summarizing the results, it can be stated that gQED performed well, producing similar over-all results as the reference SPM. Deviations in T-statistics were only minor between the smoothing methods, increases originally expected with gQED were not observed due to increased data variance with this smoothing approach. Instead, a large dependency of T-statistics on normalization procedure was observed.

8.1 Normalization

Deficiencies in volumetric normalization are certainly known to the neuroimaging community and promote the creation of novel and more advanced normalization procedures. Direct comparisons of several spatial normalization procedures especially regarding functional data seem to be sparse, though [38]. The author of this thesis suggests that little research on this topic, though, may be rooted in the often overlooked importance of normalization in combination with smoothing of functional data: In functional images which have been smoothed with a simple volumetric kernel resulting in reduced resolution, for similar normalization procedures only little influence on activation can be observed. In Fig. 26 one can easily see that differences in functional data analysis with different normalization procedures are much more pronounced with increasing image resolution/reduced FWHM. As CVS-normalization differs significantly from SPM-normalization, differences in activation were well-visible with Gaussian smoothing.

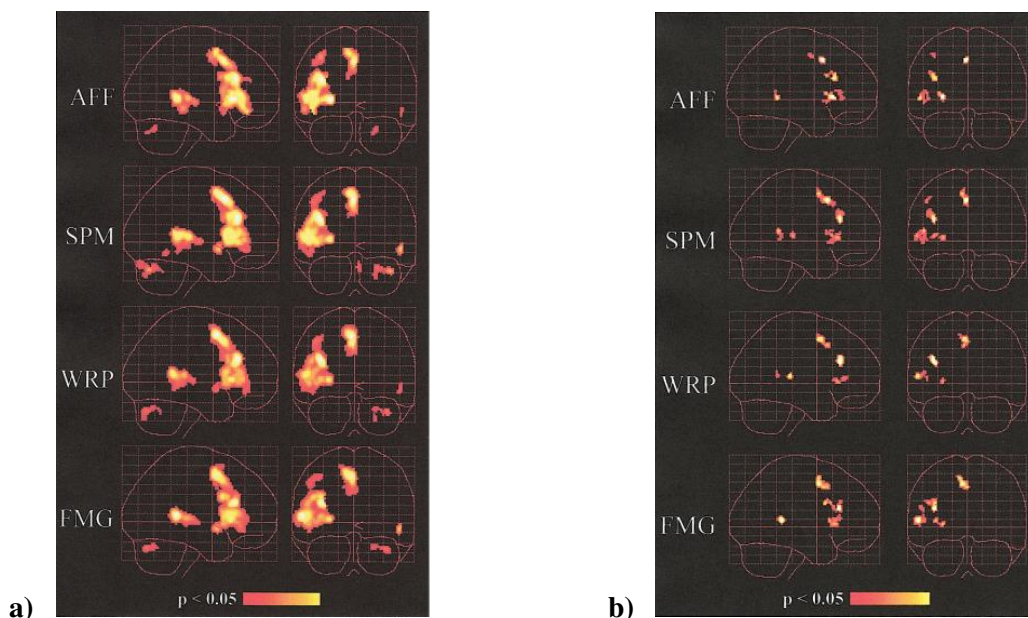


Fig. 26 Impact of spatial normalization procedures on “low resolution” (a) and “high resolution” (b) functional activation maps; adapted from [38].

The appearance of limitations caused by insufficient normalization was expected to some degree especially when using restrictive masks. The major influence of different normalization procedures

on the results – both on statistics and location of the activation – was surprising to the author and can be regarded as an accidental but nevertheless very important finding of this thesis work.

As can be seen in Table 7 using CVS instead of SPM's standard normalization procedure led to a major increase in the maximum T-value of the motor-associated activation cluster (SPM-smoothing: +16.8%, gQED-smoothing: +8.5%) and a shift of the cluster maximum by 24 mm towards the brain's surface. Even the spatially closest local maximum in the CVS-cluster was 10.4 mm from the maximum in the SPM-cluster.

While changes in the location of activation clusters and maxima should further be investigated and verified, it can be concluded that such major increases in T-statistics (significance of the activation) as caused by CVS-normalization facilitates the identification of activated areas which would otherwise falsely remain undetected. In e.g. [39] the influence of normalization procedures on activation detectability and the importance of reduced inter-subject anatomical variability for detection of spatially small activation patterns has been previously reported as well.

8.1.1 GM Overlap

Fig. 20 c) and d) show the normalized, segmented and summed anatomical scans for CVS- and SPM-normalization. Except for the cerebellum in the lower part of the brain much better spatial overlap is achieved with CVS as can be deduced from the relatively uniform color and well-visible gyration. In [8] CVS is also reported to outperform accuracy and robustness of the two further well-known registration methods FLIRT [40] and HAMMER [41], with FLIRT being claimed to achieve better normalization than SPM (SPM99) [41].

Additionally, when a restrictive mask was used to smooth the CVS-normalized data the resulting statistics are still very close to the SPM-normalized ones, even though the restrictive mask includes only a fraction of voxels. If single-subject data were severely compromised by the restrictive mask the numbers would be expected to drop by a larger extent.

8.1.2 Spatial Signal Separation

Another result in the favor of CVS-normalization is shown in Fig. 21: The activation pattern shows more refined internal structure (local maxima) and matches the template's anatomy better, since maxima spatially match gyri. Some caution needs to be applied when using this argument, though: If a signal originated on one side of a narrow sulcus an activation cluster in the middle of a sulcus might better represent the true activation site than a 'blob' in the middle of the correct gyrus showing no trend towards one of the gyri's sides or local maxima in both gyri forming the sulcus.

8.2 Smoothing

8.2.1 Masking and Crosstalk

A major advantage in using surface-based smoothing and thus also gQED with a restrictive mask is reduced or even complete lack of signal-mixing from different tissues and neighboring gyri. [42]

In Fig. 24 the contrasts resulting from surface-based analysis for a single subject shows the majority of activation located in the post-central gyrus. Fig. 18 on the other hand seems to show more activation for the single subject in the pre-central gyrus, which is more consistent with the theoretically expected result from the paradigm and with the group results (Fig 25). This may be attributed to imperfections in masking and coregistration of anatomical and functional scans in the FS-FAST workflow.

Hemispheres, in contrast to gyri, should be rather well-separable by masking. In Fig. 22 one can see activation in the supplementary motor center. When no mask is applied the activation pattern spreads from the left hemisphere to the right hemisphere across the longitudinal fissure. Looking at the cluster maximum's location and knowing the task performed it is reasonable to assume that activation should be located rather only in the left supplementary motor center. When a restrictive mask is applied and gQED-smoothing is used, indeed no or only negligible small activation in the right supplementary motor area is seen. This is not the case with SPM-smoothing and the restrictive mask, as SPM does smooth across the masked longitudinal fissure.

It must be added that masking in volume space or projection to surface space may not necessarily completely separate signals and restrict them to their true location [42]. Even with perfect detection of anatomical features and perfect coregistration this could not be achieved, simply because there is some spatial extent of the measured BOLD-signal. E.g. when lowering the threshold of the gQED-processed data so that less robust effects are also shown (uncorrected p-values), activation in the right supplementary motor area can also be seen.

Concluding, gQED's masking and smoothing abilities may provide interesting insights in future applications, especially when the exact location of activation is of utmost importance (e.g. in neurosurgery) or when investigating lateralization effects.

Although corresponding data is not presented here as this would exceed the scope of this work it shall be added that possible effects of masking on multiple comparison correction were explored by additionally using two further statistical methods (TFCE and SnPM) which do not depend on random field theory and thus smoothness estimates. Any differences – if they could be observed at all – were small enough to be considered insignificant.

8.2.2 Signal Magnitude and Variability

Functional analysis can be boiled down to two numbers: effect strength (beta) and statistical significance of activation (T).

While T being larger than the threshold calculated in multiple comparison correction is sufficient for activation to be declared as significant, a large value of course is preferable. If values generally increase for a different smoothing method, the results can be considered as more reliable and one can also expect to be able to detect locations which originally fell below the threshold.

Large effect strength is not necessarily needed for large T-values (see eq. (26)), but of course a larger effect can be detected more easily among noise.

Analysis of time courses (Fig. 14 and Fig. 17), beta- and T-values (Fig. 14 and Fig. 19) and SNR (Fig. 16 and Fig. 17) both for artificial signals as well as experimental data led to the following observations: Compared to SPM-smoothed data, using gQED results in increased single-subject effect strength at lower SNR. This is easily explained by less 'irrelevant' data (white matter, CSF, air...) being mixed with the relevant signal changes. Single-subject T-statistics are roughly equivalent as well as group statistics, though. Since group-level T-values depend on single-subject effect strength (beta) this may seem counter-intuitive at first. Upon closer inspection gQED-smoothed data is afflicted with larger variability and thus variance as visible in the boxplots in Fig. 19. Since

$$T = \frac{\text{effect}}{\text{variance}} \quad (26)$$

a roughly constant T resulting from higher con-values can only be achieved with larger variance.

8.2.3 Activation Detection and Localization

Independent of the volumetric smoothing method, when the same data (i.e. identical preprocessing prior to smoothing) and masks were used, location of absolute maxima in activation for a single anatomical region typically did not differ or variation was only minor (range of 2 mm, which equals one voxel). Changes in the location and relative magnitude of local maxima within the anatomical region were observed, though.

Different normalization procedures resulted in large (Euclidean) distances between the respective motor-cortex maxima, ranging from 15-25 mm. This is also visible comparing normalization implemented in SPM and normalization in also well-established but less commonly used FreeSurfer.

The number of available processing tools and pipelines in general and especially in combination with the lack of a gold-standard for functional analysis has been previously identified as problematic regarding comparability in detected activation locations and patterns. [43]

Further observations included maximum T-statistics being similar between SPM and gQED for the same normalization procedures and T-statistics being larger for SPM and gQED than for FreeSurfer, assumed to be rooted in the small volume being projected to the surface. Visual comparison showed gQED clusters commonly being more refined and slightly smaller than the corresponding clusters in SPM.

8.2.4 Computational Performance

Computers get more and more powerful, both decreasing time needed for mathematical operations as well as making storage and working with large amounts of data possible. On the other hand research budgets are often limited and infrastructure needed is expensive. Therefore, timely results even on older hardware are advantageous if one wants to introduce novel analysis procedures.

8.2.4.1 Hardware

Computations were done on the NIL servers (12 cores, 56 GB RAM), running CentOS 6.4 with MATLAB R2018b and FreeSurfer 6.0.0 installed. Due to Covid-19 related access restrictions, temporarily two personal laptop computers were used in parallel, running MATLAB R2019b on Windows 10 with 8 and 12 GB RAM, respectively. When restrictions were revoked, all data was reanalyzed on the NIL servers (except for aws4SPM analyses due to software availability). Although no relevant differences are to be expected, this way any deviations introduced by software versions can be excluded.

As a positive side-effect of home-office, it could be shown that gQED performs without problems on different operating systems and on rather low-end hardware. Parallelization on a laptop computer is a challenge, though and the server ran much faster.

8.2.4.2 Runtime

8.2.4.2.1 gQED & SPM

Depending on mask size/threshold, as well as FWHM used (and/or stored) the time needed for gQED-smoothing of a single subject (4D volume: 79x95x69x95) varied between roughly 5.5 and 20 minutes. In contrast, smoothing with SPM is mask-invariant and took 1 to 2 minutes per subject. Roughly, an increase in smoothing time of a factor 10-20 when switching from SPM to gQED can be expected.

Calculating geodesic distances needed for smoothing also largely depends on the number of mask voxels and FWHM (i.e. max distances to be calculated). Time needed was in the range of one to two hours. However, if the same mask and same or smaller FWHM is used for other studies, the intracortical distances can be stored and only need to be calculated once.

8.2.4.2.2 FreeSurfer

While smoothing in surface space on its own takes little time it is dependent on time-consuming prior processing steps. These take much longer than the same preprocessing steps in volume space, easily exceeding 10 hours per subject. Thus, group analysis is only viable if subjects are processed in parallel using multiple CPU cores. This makes surface-based analyses less attractive when processing time and hardware requirements are to be kept low.

CVS-normalization is dependent on preprocessing steps of anatomical data in FreeSurfer and additionally needed more than a day per subject to compute the spatial normalization from subject data to template space.

8.3 Limitations

8.3.1 Masking

A wide variety of anatomical masks has been tested throughout data acquisition for this thesis work. Best group-results by means of T-values were achieved with a “full brain” mask (voxels with the sum of WM, GM and CSF probability $\geq 50\%$ are included) with voxels of WM-probability $\geq 90\%$ excluded.

When looking back at Fig. 20 it is not surprising that statistics on group level worsened considerably with restrictive masking when normalization was not optimal. The high level of anatomical differences left after spatial normalization with SPM was unexpected, though.

Of course, the mask’s shape and the threshold used can have a major influence on the results and may even bias them e.g. by false negatives or moving of activation maxima when areas of activation are excluded for some subjects. It has also to be kept in mind that even with high GM-probability thresholds not all gyri and sulci are well resolved. Thus, in some cases it might be advisable to manually correct a mask by including or excluding certain voxels to better follow brain anatomy.

While crosstalk between two areas can be completely restricted with masking and gQED, one should not forget that some signal may have been allocated to the uninvolved area during data acquisition or processing-steps prior to smoothing. This is especially the case for low-resolution images.

8.3.2 CVS-Normalization

Anatomical variability between subjects is a critical limitation for statistical analyses of groups [39], especially when one wants to use restrictive masks.

While CVS-normalization had a major positive effect on SPM analyses as well as gQED analyses of the real finger-tapping dataset, this normalization approach applied to functional data is still uncommon in the imaging community. As a result, neither directly comparable datasets have been found nor reports on localization changes induced by this procedure and its overall reliability. Changes in the location of activation in general when using different normalization procedures have been previously reported, though [38].

A major drawback of CVS-normalization is its long processing time, especially since it succeeds FreeSurfer's already time-consuming segmentation. This may result in reluctant use of this method despite its advantages. In addition, further reasons limiting the number of users may be the need for additional software and the resulting learning curve, the lack of a graphic user interface for FreeSurfer and CVS and reduced comparability with previous studies where purely volumetric normalization procedures had been used. Using older, less precise methods out of habit and for the sake of easy comparison was also suggested as an explanation to why surface-based analysis is barely used [44].

8.3.3 Software - Licenses

gQED and more specifically its geodesic distance calculation depends on MATLAB's Image Processing Toolbox, as they use the functions *bwdistgeodesic*. This toolbox is neither freely available nor included in standard MATLAB distributions, but can be assumed to be widely distributed and used in the medical imaging community. It would be possible, though, to provide mask files and inter-voxel distances, whose usage does not depend on toolboxes.

Freesurfer, SPM and aws4SPM are all freely available, but may depend on MATLAB or MATLAB toolboxes.

8.4 Other Smoothing Approaches

As many other approaches tackling aforementioned limitations in volumetric smoothing exist, a short overview on two further selected methods will be given.

8.4.1 Anatomically Informed Basis Functions

Kiebel et al. proposed the concept of anatomically informed basis functions (AIBF) in 2000 as an alternative voxel-based fMRI-analysis approach. Among their framework's features are a smoothing kernel depending on location, allowing smoothing along the cortical surface, and a possibility for super-resolution since the surface is reconstructed at sub-voxel-resolution. [45]

The AIBF procedure includes extraction and reconstruction of cortical surfaces, specifying a transformation between vertex-space intensities and voxel-space signal and defining and (re)projecting basis functions on cortical sheet and cortex surface in voxel-space, respectively. Basis functions may be hexagonally arranged (in vertex-space) circular Gaussian functions with an additional Gaussian in the center of each hexagon. Transformation to voxel space is then applied.

Although higher sensitivity for GM-signals reported than achieved with SPM-smoothing, this method does not seem to have been widely disseminated or applied.

8.4.2 Gaussian Processes

Gaussian processes (GP) have been implemented in fMRI data smoothing rather recently. For details the interested reader is referred to e.g. [46]. GP regression is a nonparametric Bayesian method originally applied in machine learning. When used for fMRI smoothing, noise and the spatiotemporal characteristics of BOLD-responses are analyzed, and the smoothing kernel is adapted according to these findings for each voxel.

It is reported, that with GP smoothing both higher sensitivity and specificity can be achieved on subject-level, whereas common volumetric smoothing increases sensitivity at the cost of specificity [46].

Although some MATLAB code was provided online, this method was not further pursued in the analysis presented here, as the code was lacking documentation and not all necessary files were available. Using subject- and voxel-specific smoothing is also problematic as this yields different degrees of freedom for group analysis.

8.5 Possible Enhancements and Outlook

8.5.1 Computation Time and Memory Requirements

Even when considering only short distances, calculation of geodesic distances between any two voxels within the gray matter is a lengthy process. Theoretically, the time needed, as well as memory required, could be noticeably decreased, if one considered path- or rather distance symmetry between voxels:

Let the distances d from seed v_a to its neighbors be

$$d(v_a) = \begin{pmatrix} \vdots \\ d_{a,i} \\ d_{a,j} \\ d_{a,k} \\ \vdots \end{pmatrix} \quad (27)$$

As

$$d_{a,i} \stackrel{!}{=} d_{i,a} \quad (28)$$

$$d(v_i) = \begin{pmatrix} d_{i,a} \\ \vdots \\ d_{i,j} \\ d_{i,k} \\ \vdots \end{pmatrix} \quad (29)$$

contains not as much information as $d(v_a)$ if $d(v_a)$ is already known, but contains one redundant entry. Theoretically, it would be sufficient to store a sparse matrix only, such as

$$d = \begin{pmatrix} \cdot & \cdot & \cdot & \cdot \\ d_{1,2} & \cdot & \cdot & \cdot \\ d_{1,3} & d_{2,3} & \cdot & \cdot \\ d_{1,4} & d_{2,4} & d_{3,4} & \cdot \\ \vdots & \vdots & \vdots & \ddots \end{pmatrix} \quad (30)$$

To this date, an already existing, time-saving implementation of geodesic distance calculation is neither known to the author, nor has been coded by the author during this thesis as this would exceed its scope. While large benefits regarding the time needed for calculating the distances in the first place are to be expected for a non-redundant geodesic-distance algorithm, it is questionable, whether and to what degree one would benefit on the scale of the whole analysis from storing the distances in such a sparse matrix for several reasons:

- In MATLAB, there is no protocol for storing only the lower triangular section of a matrix.
- Using a sparse matrix is only less memory consuming if the matrix consists of sufficient zero-entries. `sparse(A)` converts the full matrix A to a list of matrix coordinates and the corresponding value. Each non-zero element of a 2D matrix A thus will be stored as coordinates x and y plus the value at $A(x,y)$. Saving the linear index and the corresponding value needs even less memory. To cite MATLAB's documentation:

“If the order of a matrix is small enough that full storage is possible, then conversion to sparse storage rarely offers significant savings.”

- The benefit of requiring less disc space to store masks and the geodesic distances between voxels might be outweighed by increasing processing steps needed and increasing computation time for smoothing. As an anecdote, an attempt to reduce the number of loops in the code and further vectorize calculations led to a major increase in calculation time, as it included setting up and manipulating larger and higher-dimensional matrices.
- As large RAMs and hard drives become more easily available, memory requirements become of less importance.

8.5.2 Further Applications

gQED smoothing as well as CVS-normalization may be promising tools for image analysis. gQED is easy to replicate and implement into existing preprocessing pipelines. Although its influence on overall calculation time is considerable compared to classic spatial smoothing, it may prove valuable e.g. as a fast and easily adaptable replacement of surface-based analysis.

8.5.2.1 High-Resolution fMRI

BOLD fMRI resolution is typically rather low, especially compared to resolutions used in anatomical scans. Although higher resolution could often be achieved with modern scanners, this would result in lower SNR, which then requires more smoothing (i.e. larger kernel FWHM) eliminating the spatial detail gained during acquisition. Escaping this vicious cycle is partially possible by smoothing methods which follow anatomy and tissue borders [29]. gQED can achieve this and higher resolution and smaller voxel size will also reduce problems in masking. Therefore, testing gQED on high-resolution fMRI seems like a promising field of application. The only downside and limiting factor may be the additional memory needed to store the increasing number of voxel indices and corresponding distances.

8.5.2.2 Increased Specificity

As already explained, geodesic smoothing in well-defined masks prevents crosstalk. When signals from unrelated areas in close proximity are no longer mixed during smoothing, advances in activation specificity are to be expected, as the areas' time courses remain independent from each other. This may also apply to the field of functional connectivity, which computes cross-correlations between voxels' time courses. Similar to activation analyses, it is important for connectivity calculations that a voxel's signal is not influenced by its surrounding tissue [42].

8.5.2.3 Test-Retest & Longitudinal Studies

In longitudinal and test-retest studies single subjects perform an identical task at two or more different times and changes between the sessions are analyzed.

With longitudinal and test-retest studies conclusions on variability in measurement processes, cognition per se and on alterations in brain physiology due to pharmaceutical interventions, learning processes, illnesses etc. can be drawn. See e.g. [47] and [48] for the discussion of within-subject variability in fMRI when the same subject repeats the same task during several measurements.

Performance of gQED on these data seems promising as variance caused by imperfect spatial normalization and smoothing could be reduced. Furthermore, no time-consuming CVS-normalization would be needed to still be able to work with a restrictive mask.

8.5.2.4 *WM-Activation*

In its current form, gQED smooths GM-signal and gets rid of any signal in high-WM-probability areas. As reported in [49], whilst the signals are much smaller, also activation in WM and deeper brain structures (especially in the corpus callosum) may frequently be observed during tasks. Currently, these activations are rarely in the focus of research, but may become of increasing interest. By substituting the applied mask, gQED could easily be adapted to analyze WM instead.

8.5.2.5 *Other imaging modalities*

Finally, it should be emphasized that the implemented processing pipelines will be equally applicable to other imaging modalities which need spatial smoothing. This includes e.g. data from PET, ASL and structural imaging, whose results may improve in a similar manner.

9 Conclusion

A smoothing algorithm for 3D/4D-images using geodesic, quasi-Euclidean distances (gQED) has been proposed, implemented and compared to various other image smoothing and analysis methods. Such a method could provide the imaging community with a versatile tool bridging the gap between purely volumetric and purely surface-based smoothing.

For both, simulated and experimental data, gQED delivered comparable T-values (activation significance) at single-subject and group- analysis, with increased effect strength but also variability. SNR was slightly reduced when using gQED.

As a major advantage, gQED with proper restrictive masking will only smooth data within the gray matter but not across anatomical or tissue boundaries, thus preventing partial volume effects and crosstalk between spatially close but functionally distinct brain regions.

Interestingly, in experimental data such a restrictive masking was only applicable for the time-consuming but high-quality spatial normalization (CVS). Thus, the work also highlighted previously unknown or disregarded deficiencies in SPM's spatial normalization procedure.

To summarize gQED proved

- to be easy to implement into voxel-wise processing pipelines
- to reproduce locations of neuronal activations at least as well as the widely used SPM toolbox
- to deliver comparable statistical results of neuronal activations in the motor cortex when compared to SPM and higher T-values than FreeSurfer with manageable memory and time restraints.

Thus, the approach may serve as a relevant tool to provide accurate identification of neuronal activation in the human brain.

10 References

- [1] A. Andrade, F. Kherif, J. F. Mangin, K. J. Worsley, A. L. Paradis, O. Simon, S. Dehaene, D. Le Bihan and J. B. Poline, "Detection of fMRI activation using Cortical Surface Mapping," *Human Brain Mapping*, vol. 12, no. 2, pp. 79-93, 2 2001.
- [2] D. W. McRobbie, E. A. Moore and M. J. Graves, *MRI from Picture to Proton*, 3rd Edition ed., New York: Cambridge University Press, 2017.
- [3] R. Ansorge and M. Graves, *The Physics and Mathematics of MRI*, San Rafael, CA: Morgan & Claypool Publishers, 2016.
- [4] R. A. Poldrack, J. A. Mumford and T. E. Nichols, *Handbook of Functional MRI Data Analysis*, New York: Cambridge University Press, 2011.
- [5] C. Clarke, S. Abdulla and M. Sia, "Radiology Café," 17 July 2020. [Online]. Available: <https://www.radiologycafe.com/radiology-trainees/frcr-physics-notes/t1-t2-and-pd-weighted-imaging>. [Accessed 10 October 2020].
- [6] M. K. Chung, S. M. Robbins, K. M. Dalton, R. J. Davidson, A. L. Alexander and A. C. Evans, "Cortical thickness analysis in autism with heat kernel smoothing," *NeuroImage*, vol. 25, no. 4, pp. 1256-1265, 1 5 2005.
- [7] A. Anticevic, D. L. Dierker, S. K. Gillespie, G. Repovs, J. G. Csernansky, D. C. Van Essen and D. M. Barch, "Comparing surface-based and volume-based analyses of functional neuroimaging data in patients with schizophrenia," *NeuroImage*, vol. 41, no. 3, pp. 835-848, 2008.
- [8] G. Postelnicu, L. Zöllei and B. Fischl, "Combined Volumetric and Surface Registration," *IEEE Transactions on Medical Imaging*, vol. 28, no. 4, pp. 508-522, April 2009.
- [9] M. Welvaert, K. Tabelow, R. Seurinck and Y. Rosseel, "Regions, Adaptive Smoothing as Inference Strategy," *Neuroinform*, vol. 11, pp. 435-445, 2013.
- [10] H. J. Jo, J. M. Lee, J. H. Kim, C. H. Choi, B. M. Gu, D. H. Kang, J. Ku, J. S. Kwon and S. I. Kim, "Artificial shifting of fMRI activation localized by volume- and surface-based analyses," *NeuroImage*, vol. 40, no. 3, pp. 1077-1089, 15 4 2008.
- [11] M. M. Monti, "Statistical analysis of fMRI time-series: a critical review," *Frontiers in Human Neuroscience*, vol. 5, no. 28, pp. 1-13, 2011.
- [12] S. Aja-Fernández and G. Vegas-Sánchez-Ferrero, *Statistical Analysis of Noise in MRI: Modeling, Filtering and Estimation*, Springer International Publishing Switzerland, 2016.
- [13] G. Krüger and G. H. Glover, "Physiological Noise in Oxygenation-Sensitive Magnetic," *Magnetic Resonance in Medicine*, vol. 46, no. 4, pp. 631-637, 2001.
- [14] A. Scouten, X. Papademetris and R. T. Constable, "Spatial resolution, signal-to-noise ratio, and smoothing in multi-subject functional MRI studies," *NeuroImage*, vol. 30, no. 3, pp. 787-793, 2006.

- [15] T. A. Yousry, U. D. Schmid, H. Alkadhi, D. Schmidt, A. Peraud, A. Buettner and P. Winkler, "Localization of the motor hand area to a knob on the precentral gyrus; A new Landmark," *Brain*, vol. 120, pp. 141-157, 1997.
- [16] J. Betts, P. Desaix, E. Johnson, J. E. Johnson, O. Korol, D. Kruse, B. Poe, J. A. Wise, M. Womble and K. A. Young, "OpenStax," Rice University, 2017. [Online]. Available: <https://openstax.org/details/books/anatomy-and-physiology>. [Accessed 7 October 2020].
- [17] J. Morrison, "From Neurone to Nervous System," 2017. [Online]. Available: <http://neurones.co.uk/Neurosciences/Tutorials/M4/M.4.1a%20Cortex%20Methods.html>. [Accessed 7 October 2020].
- [18] M. Welvaert and Y. Rosseel, "A Review of fMRI Simulation Studies," *PLoS ONE*, vol. 9, no. 7, July 2014.
- [19] J. Manning, "MATLAB Central File Exchange," 2020. [Online]. Available: <https://www.mathworks.com/matlabcentral/fileexchange/36125-generate-synthetic-fmri-data>. [Accessed 17 02 2020].
- [20] H. J. Jo, J. M. Lee, J. H. Kim, Y. W. Shin, I. Y. Kim, J. S. Kwon and S. I. Kim, "Spatial accuracy of fMRI activation influenced by volume- and surface-based spatial smoothing techniques," *NeuroImage*, vol. 34, no. 2, pp. 550-564, 15 1 2007.
- [21] E.-J. Hwang, M.-J. Kim and G.-H. Jahng, "Gaussian Filtering Effects on Brain Tissue-masked Susceptibility Weighted Images to Optimize Voxel-based Analysis," *Journal of the Korean Society of Magnetic Resonance in Medicine*, vol. 17, no. 4, p. 275, 2013.
- [22] J. Pajula and J. Tohka, "Effects of spatial smoothing on inter-subject correlation based analysis of fMRI," *Magnetic Resonance Imaging*, vol. 32, no. 9, pp. 1114-1124, 2014.
- [23] M. X. Cohen, *MATLAB for Brain and Cognitive Scientists*, Cambridge: MIT Press, 2017, p. 193 ff.
- [24] J. Carp, "The secret lives of experiments: Methods reporting in the fMRI literature," *NeuroImage*, vol. 63, no. 1, pp. 289-300, 2012.
- [25] P. Soille, *Morphological Image Analysis: Principles and Applications*, 2nd Edition ed., Secaucus, NJ: Springer Verlag, 2003, pp. 219-221.
- [26] B. Kraus, "MATLAB Central File Exchange," 16 October 2020. [Online]. Available: <https://www.mathworks.com/matlabcentral/fileexchange/41961-nanconv>. [Accessed 10 February 2020].
- [27] J. Polzehl, H. U. Voss and K. Tabelow, "Structural adaptive segmentation for statistical parametric mapping," *NeuroImage*, vol. 52, no. 2, pp. 515-523, 2010.
- [28] J. È. Polzehl and V. G. Spokoiny, "Adaptive weights smoothing with applications to image restoration," *Journal of The Royal Statistical Society Series B-statistical Methodology*, vol. 62, pp. 335-354, 2000.
- [29] K. Tabelow, V. Piëch, J. Polzehl and H. U. Voss, "High-resolution fMRI: Overcoming the

- signal-to-noise problem," *Journal of Neuroscience Methods*, vol. 178, no. 2, pp. 357-365, 15 4 2009.
- [30] A. M. Dale, B. Fischl and M. I. Sereno, "Cortical Surface-Based Analysis; I. Segmentation and Surface Reconstruction," *NeuroImage*, vol. 9, no. 2, pp. 179-194, February 1999.
- [31] B. Fischl, M. I. Sereno and A. M. Dale, "Cortical Surface-Based Analysis; II: Inflation, Flattening, and a Surface-Based Coordinate System," *NeuroImage*, vol. 9, no. 2, pp. 195-207, February 1999.
- [32] B. Fischl, M. I. Sereno, R. B. Tootell and A. M. Dale, "High-Resolution Intersubject Averaging and a Coordinate System for the Cortical Surface," *Human Brain Mapping*, vol. 8, no. 4, pp. 272-284, 1999.
- [33] B. Fischl, "Freesurfer," *Neuroimage*, vol. 62, no. 2, pp. 774-781, August 2012.
- [34] D. N. Greve, C. Svarer, P. M. Fisher, L. Feng, A. E. Hansen, W. Baare, B. Rosen, B. Fischl and G. M. Knudsen, "Cortical surface-based analysis reduces bias and variance in kinetic modeling of brain PET data," *NeuroImage*, vol. 92, pp. 225-236, 2014.
- [35] A. Klein and J. Tourville, "101 Labeled Brain Images and a Consistent Human Cortical Labeling Protocol," *Frontiers in neuroscience*, vol. 6, p. 171, 2012.
- [36] L. Rischka, G. Gryglewski, S. Pfaff, T. Vanicek, M. Hienert, M. Klöbl, M. Hartenbach, A. Haug, W. Wadsak, M. Mitterhauser, M. Hacker, S. Kasper, R. Lanzemberger and A. Hahn, "Reduced task durations in functional PET imaging with [18 F]FDG approaching that of functional MRI," *NeuroImage*, 2018.
- [37] D. Hoffmann and K. Tabelow, "Structural adaptive smoothing for single-subject analysis in SPM: the aws4SPM-toolbox," *WIAS Technical Report*, vol. 11, 2008.
- [38] F. Crivello, T. Schormann, N. Tzourio-Mazoyer, P. E. Roland, K. Zilles and B. M. Mazoyer, "Comparison of Spatial Normalization Procedures and Their Impact on Functional Maps," *Human Brain mapping*, vol. 16, pp. 228-250, 2002.
- [39] A. M. Tahmaseb, P. Abolmaesumi, Z. Z. Zheng, K. G. Munhall and I. S. Johnsrude, "Reducing Inter-subject Anatomical Variation: Effect of Normalization Method on Sensitivity of Functional Magnetic Resonance Imaging Data Analysis in Auditory Cortex and the Superior Temporal Region," *NeuroImage*, vol. 47, no. 4, pp. 1522-1531, October 2009.
- [40] M. Jenkinson, P. Bannister, M. Brady and S. Smith, "Improved optimisation for the robust and accurate linear registration and motion correction of brain images," *NeuroImage*, vol. 17, no. 2, pp. 825-841, 2002.
- [41] D. Shen and C. Davatzikos, "HAMMER: Hierarchical Attribute Matching Mechanism for Elastic Registration," *IEEE TRANSACTIONS ON MEDICAL IMAGING*, vol. 21, no. 11, pp. 1421-1439, 2002.
- [42] S. Brodoehl, C. Gaser, R. Dahnke, O. W. Witte and C. M. Klingner, "Surface-based analysis increases the specificity of cortical activation patterns and connectivity results," *Scientific*

Reports, vol. 10, no. 15737, 2020.

- [43] A. Bowring, C. Maumet and T. E. Nichols, "Exploring the impact of analysis software on task fMRI results," *Human Brain Mapping*, vol. 40, pp. 3362-3384.
- [44] T. S. Coalson, D. C. Van Essen and M. F. Glasser, "The impact of traditional neuroimaging methods on the spatial localization of cortical areas," *PNAS*, vol. 115, no. 27, pp. 356-365, 2018.
- [45] S. J. Kiebel, R. Goebel and K. J. Friston, "Anatomically informed basis functions," *NeuroImage*, vol. 11, no. 6 I, pp. 656-667, 2000.
- [46] F. Strappini, E. Gilboa, S. Pitzalis, K. Kay, M. McAvoy, A. Nehorai and A. Z. Snyder, "Adaptive smoothing based on Gaussian processes regression increases the sensitivity and specificity of fMRI data," *Human Brain Mapping*, vol. 38, no. 3, pp. 1438-1459, 1 3 2017.
- [47] D. J. McDonigle, A. M. Howseman, B. S. Athwal, K. J. Friston, R. S. Frackowiak and A. P. Holmes, "Variability in fMRI: An Examination of Intersession Differences," *NeuroImage*, vol. 11, no. 6, pp. 708-734, June 2000.
- [48] M. Raemaekers, S. du Plessis, N. F. Ramsey, J. M. Weusten and M. Vink, "Test–retest variability underlying fMRI measurements," *NeuroImage*, vol. 60, pp. 717-727, 2012.
- [49] J. R. Gawryluk, E. L. Mazerolle and R. C. N. D'Arcy, "Does functional MRI detect activation in white matter? A review of emerging evidence, issues, and future directions," *Frontiers in Neuroscience*, vol. 8, p. 239, 2014.

11 Table of Figures

Fig. 1 Schematic description of spatial smoothing: left: exemplary gyri (GM: dark gray, WM: light gray) and sulci (CSF: black), middle: smoothing by Euclidean distance as most commonly used, right: smoothing by geodesic distance as proposed in this work.	9
Fig. 2 Top left: hemodynamic response function (HRF) schematic: ID ... initial dip; TP ... time from stimulus to peak; W ... width at half height; PSU ... post-stimulus undershoot ; Lower left: BOLD fMRI series: stimulus (red) and corresponding response (blue); Top right: Signal for different neural response magnitude; Lower right: Approximately linear response of BOLD for several stimuli within short time interval; Composition of several figures from [4]	12
Fig. 3 Slice Time Correction: a) slice order for interleaved acquisition; b) corresponding signals; Later acquired slices appear to exhibit an earlier response, as they do not detect the true onset of the HRF; Taken from [4].....	13
Fig. 4 GLM-schematic taken from [11]: A BOLD time-course is predicted by three tasks and seven nuisance regressors.....	16
Fig. 5 Noisy image: left to right: data acquisition to final image; σ^2 ... Variance; $ \Omega $... Size of Field of View (number of points in 2D inverse discrete Fourier transform); For large SNR the signal can be estimated as Gaussian distributed, for SNR = 0 (i.e. image background) the Rician distribution simplifies to a Rayleigh distribution; Taken from [12].....	16
Fig. 6 Noise contributions as depicted and described in [13]: “Anatomy (a) and spatial distribution of raw noise σ_0 (b), physiological noise contributions σ_B (c), and σ_{NB} (d) in a typical image section from one subject. Note that gray scale contrast is identical in b–d .”	18
Fig. 7 Location of left motor hand area on the MNI152 template, localized as described in [15]: “The segment of the precentral gyrus that most contained motor hand function was a knob-like structure, that is shaped like an omega or epsilon in the axial plane and like a hook in the sagittal plane.”	18
Fig. 8 Primary motor cortex: Sensory homunculus: Left: Coronal view (Source: [16]) Right: Lateral view, Penfield’s map (Source: [17])	19
Fig. 9 Artificial signal created by convolution of HRF and design matrix (‘Task’). Left: time course; Right: Single frame (time instance) of the resulting simulated BOLD-measurement shown in coronal, sagittal and axial slices. Activation (increased simulated BOLD-values) is slightly visible in the brain’s left hand-motor center as a small white batch of higher intensity than the surrounding tissue, the location is indicated by arrows.....	20
Fig. 10 Isosurface plots for distance transforms of a 3D-image; Image dimensions [50 50 50]; There is a single non-zero voxel at [25 25 25]; Each isosurface displays a distance of 15 units using the metric specified in the subplot’s title. Image taken from MATLAB Documentation for function <code>bwdist()</code>	25
Fig. 11 Differences in voxel intensities for different smoothing approaches; left column: results of smoothing a single voxel of $I = 100$ with different kernels and metrics; right column: smoothed	

image obtained by various methods subtracted from SPM-result. Please note the different scaling of the right column. 26

Fig. 12 Inflated surface representation of the human brain; **Left and center:** color-coded template brain prior and post inflation, sagittal cross section of pre- and postcentral gyrus depicted below; Adapted from [35] **Right:** Color coded gyri and sulci on inflated brain; Adapted from andysbrainbook.readthedocs.io 28

Fig. 13 Multi-planar views: Coronal, sagittal and axial slices of several gray matter probability-maps; **a & b:** Exemplary selection of thresholds t_p and the resulting GM-mask of a TPM; **c:** MNI152 template-derived GM mask; **d:** custom mask derived by combining several tissue thresholds ('Fullbrain' - $t_{WM} > 0.9$); **e:** GM-segmentation derived from a single subject's anatomical scan 30

Fig. 14 Artificial BOLD-signal time courses ; **Top left:** Signal with and without added noise; **Top right:** Non-noisy signal post smoothing (SPM and gQED, no time course returned by aws4SPM-procedure); **Lower left:** Smoothed noisy signal; **Lower right:** Statistics for seed voxels. Remark: Due to large noise components and resulting signal variability the seed did not always exhibit the largest T-value..... 32

Fig. 15 Statistically relevant activation patterns (thresholded T-statistics) for different smoothing methods (left to right: SPM, gQED, aws4SPM) of an artificial BOLD-signal. **Top row:** T-statistics for non-noisy data (time course as in Fig. 14 top right); **Bottom row:** T-statistics for noisy data (time course as in Fig. 14 bottom left) 33

Fig. 16 Boxplot of the SNR of 20 artificial subjects prior to and post smoothing 33

Fig. 17 Single-voxel time courses of a representative subject; The chosen voxel had the highest T-statistic in this subject's statistical analysis for either normalization method..... 35

Fig. 18 Single-subject activation maps (T-statistics) with different normalization and smoothing approaches..... 36

Fig. 19 Boxplots visualizing the (pairwise) differences in magnitude of single-subject effect strength (first row) and T-statistics (second row). **Left** column: SPM-normalized data smoothed with a liberal mask; **Right** column: CVS-normalized data smoothed with a restrictive mask. Pairwise Changes visualize fractions of each subject's values derived with gQED divided by SPM-smoothed results..... 37

Fig. 20 Gray matter probability maps : **a)** TPM as distributed with SPM **b)** GM map created by segmentation of the MNI152-template using SPM **c)** scaled sum of subjects' GM maps when normalized with SPM **d)** scaled sum of subjects' GM maps when normalized with SPM..... 38

Fig. 21 Spatial differences in statistical maps derived from differently normalized data; For better visualization the same color maps were used ranging from respective T_{thresh} to T_{max} for each data set; 38

Fig. 22 Group statistics (T) of CVS-normalized data; Left to right: SPM smoothing with liberal mask, gQED smoothing in restrictive (conservative) mask, SPM-smoothing with restrictive mask; 39

Fig. 23 Activation patterns derived from different smoothing methods; Order (left to right) is the same as in Table 7 above; The coordinates show the motor cortex' maximum of activation which differ between the two normalization procedures used. Please note the differently scaled color bars which are necessary since threshold and maximum T-values varied..... 40

Fig. 24 Single subject's contrasts calculated with FS-FAST and visualized in FreeView (**left**) and a projection using mni2fs MATLAB toolbox of contrasts calculated in voxel space (gQED, subject-specific mask) on the inflated brain template (**right**). Colors and color bars show 'significances' as $-\log(p)$ 41

Fig. 25 FreeView visualizations of group-statistics calculated with FS-FAST; Colors and color bars show 'significances' as $-\log(p)$; **Left:** Data prior to multiple comparison correction; **Right:** Clusters after multiple comparison correction using random permutations..... 41

Fig. 26 Impact of spatial normalization procedures on "low resolution" (**a**) and "high resolution" (**b**) functional activation maps; adapted from [38]..... 42

12 Appendix

12.1 Acronyms and Abbreviations

AWS	Adaptive weights smoothing
BOLD	Blood oxygen level dependent (signal)
CSF	Cerebrospinal fluid
CT	Computed tomography
CVS	Combined volume and surface morph
EPI	Echo-planar imaging
fMRI	Functional magnetic resonance imaging
FS	FreeSurfer
FS-FAST	FreeSurfer functional analysis stream
FWHM	Full width half maximum
GLM	General linear model
GM	Gray matter
gQED	Geodesic quasi-Euclidean Distance (Smoothing)
HRF	Hemodynamic response function
ICA	Independent component analysis
MNI	Montreal Neurological Institute
MRI	Magnetic resonance imaging
NaN	Not a number
NIL	Neuroimaging Labs
PET	Positron emission tomography
PVE	Partial volume effect
RF	Radio frequency
sED	Smoothing: Euclidean distances
SNR	Signal-to-noise ratio
SPECT	Single photon emission computed tomography
SPM	Statistical parametric mapping (software)
sQED	Smoothing: quasi-Euclidean Distances
ST	Slice time
TE	Echo time
TPM	Tissue probability map
TR	Repetition time
WM	White matter

12.2 Code

12.2.1 Intracortical (Geodesic) Distances

```
function [storageCell] = computeDistancesV3(maskFilePath, varargin)

    maskFilePath = char(maskFilePath);
    info = niftiinfo(maskFilePath);
    pxDim = info.PixelDimensions(1);

    if info.PixelDimensions(1) ~= info.PixelDimensions(2) && ...
        info.PixelDimensions(1) ~= info.PixelDimensions(3)
        error('Pixel dimensions are not equal');
    end

    mask = niftiread(info);

    x = size(mask,1);
    y = size(mask,2);
    z = size(mask,3);

    for ii = 1:size(mask,4)

        test = zeros(x,y,z, size(mask,4));
        test(mask == 1) = 1;

        if length(find(mask)) ~= length(find(test))
            error('Are you sure your mask is defined as you want it to be?');
        end

        mask = logical(mask(:,:,,ii));

        maskIdx = find(mask);    % gets indices for masked gray matter voxels
        maskedVoxelNum = length(maskIdx);

        voxelInfo = cell(1,7);
        storageCell = cell(maskedVoxelNum, 3);

        if exist('varargin', 'var') && isscalar(varargin)
            FWHM = varargin;
        else
            FWHM = 8;
        end

        FWHM = FWHM/pxDim;
        sigma = FWHM/(sqrt(8*log(2)));

        sigmaMax = 3.5*sigma;
        dimMax = ceil(sigmaMax);

        % counter
        kk = 1;

        %% Smoothing
```

Surface-based Smoothing of Brain Imaging Data in Voxel Space

```
for jj = 1:maskedVoxelNum

    if mod(jj-1,10000) == 0                % for remaining time estimate only
        tic;
    end

    seed = false(x,y,z);                  % initialize seed voxel
    seed(maskIdx(jj)) = 1;

    voxelInfo(1,1) = {maskIdx(jj)};      % index of seed voxel

    % bwdistgeodesic is by far the slowest component of this script -->
    % since we are only interested in rather small distances, we can
    % restrict mask and image:

    [xIdx, yIdx, zIdx] = ind2sub([x,y,z], maskIdx(jj));

    if xIdx <= (dimMax+1)
        xIdxMin = 1;
    else
        xIdxMin = xIdx - dimMax;
    end

    if yIdx <= (dimMax+1)
        yIdxMin = 1;
    else
        yIdxMin = yIdx - dimMax;
    end

    if zIdx <= (dimMax+1)
        zIdxMin = 1;
    else
        zIdxMin = zIdx - dimMax;
    end

    if xIdx >= x - (dimMax+1)
        xIdxMax = x;
    else
        xIdxMax = xIdx + dimMax;
    end

    if yIdx >= y - (dimMax+1)
        yIdxMax = y;
    else
        yIdxMax = yIdx + dimMax;
    end

    if zIdx >= z - (dimMax+1)
        zIdxMax = z;
    else
        zIdxMax = zIdx + dimMax;
    end

end
```

Surface-based Smoothing of Brain Imaging Data in Voxel Space

```
maskPartial = mask(xIdxMin:xIdxMax, yIdxMin:yIdxMax, zIdxMin:zIdxMax);
seedPartial = seed(xIdxMin:xIdxMax, yIdxMin:yIdxMax, zIdxMin:zIdxMax);

temp2 = bwdistgeodesic(maskPartial, seedPartial, 'quasi-euclidean');
temp = nan(x,y,z);
temp(xIdxMin:xIdxMax, yIdxMin:yIdxMax, zIdxMin:zIdxMax) = temp2;

tempIdx = find(temp <= sigmaMax);          % set max length of interest to 3.5 stdev

voxelInfo(1,3) = {tempIdx};                % indices of other voxels
voxelInfo(1,4) = {temp(tempIdx)};         % distances to other voxels

%% smoothing with Gauss function:

storageCell(kk,1) = voxelInfo(1,1);        % seed voxel index
storageCell(kk,2) = {single(voxelInfo{1,3})}; % indices of other voxels
storageCell(kk,3) = voxelInfo(1,4);        % distances to other voxels

if jj < maskedVoxelNum
    kk = kk+1;
end

if mod(jj,1000) == 0
    if mod(jj,10000) == 0
        t10000 = toc;
        tEst = round(t10000/60*(maskedVoxelNum - jj)/10000);
        fprintf('%d of %d (%5.2f %%)... Estimated time remaining: %d min ... \n', jj,
maskedVoxelNum, (100*jj)/maskedVoxelNum, tEst);
    else
        fprintf('%d of %d (%5.2f %%)... \n', jj, maskedVoxelNum, ((100*jj)/maskedVoxelNum));
    end
end

memoryInfo = whos('storageCell');
memory = memoryInfo.bytes;

if memory >= 6500000000    % 6.5 GB
    error('WARNING: Check memory requirements. Your mask or FWHM may be too big');
end

end

filename = strcat(maskFilePath(1:end-4), '.mat');

intraCorticaldistances.storageCell = storageCell;
intraCorticaldistances.FWHM = pxDim*FWHM;
intraCorticaldistances.Mask = info.FileName;
intraCorticaldistances.PixelDimensions = info.PixelDimensions;

fprintf('Saving file. \n');
save(filename, 'intraCorticaldistances', '-v7.3');
end
```

end

12.2.2 gQED Smoothing

```
function [smoothedFramesGauss] = gQED_frame_smoothingV2(vol2smooth,storageCell, varargin)
%gQED_frame_smoothing: geodesic, quasi-euclidean-distance smoothing for the
% frames of (f)MR-data
% For the masked input volume to be smoothed (vol2smooth), the geodesic,
% quasi-euclidean distances (which have been stored in storageCell are
% used to perform voxel-wise, gaussian smoothing
%
% INPUTS: volume to be smoothed (4D), storageCell containing the
% distances between and the indices of seed and other voxels,
% FWHM (optional, default = 8mm), bool
% for neighborhood correction
%
% OUTPUTS: smoothed Volume
%
% v0.1 - 27.01.2020

%%
narginchk(2, 4);

[x,y,z, nFrames] = size(vol2smooth);

smoothedImageGauss = zeros(x,y,z,nFrames);

if nargin > 2
    FWHM = varargin{ 1 }; % [mm]
else
    FWHM = 8; % [mm]
end

FWHM = FWHM/2; % [Voxel]

sigma = FWHM/(sqrt(8*log(2)));

sigmaMax = 3.5*sigma;

if nargin == 4 && logical(varargin{2}) == 1
    neighborMatrix = ones(x,y,z);

    for jj = 1:length(storageCell)
        seedIdx = storageCell{jj,1};
        voxelIdx = storageCell{jj,2};
        temp = zeros(x,y,z);
        temp(seedIdx) = length(voxelIdx);
        neighborMatrix = neighborMatrix + temp;
    end

    neighborMatrix(neighborMatrix < 8) = nan;
end

for ii = 1: nFrames
```

Surface-based Smoothing of Brain Imaging Data in Voxel Space

```
tempImg = zeros(x,y,z);
imageFrame = vol2smooth(:,:,:,ii);

for jj = 1:length(storageCell)

    seedIdx = storageCell{jj,1};
    voxelIdx = storageCell{jj,2};
    xx = storageCell{jj,3};

    FWHM_corr = (xx <= sigmaMax);
    xx = xx(FWHM_corr);
    voxelIdx = voxelIdx(FWHM_corr);

    dd = xx.^2;

    val = imageFrame(seedIdx);

    krn = 1/(sqrt(2*pi)*sigma)^3*exp(-dd/(2*sigma^2));

    tempImg(voxelIdx) = tempImg(voxelIdx) + krn*val;
end

if nargin == 4 && logical(varargin{2}) == 1

    rescaled = tempImg./neighborMatrix;
    smoothedImageGauss(:,:,:,ii) = rescaled;

else
    smoothedImageGauss(:,:,:,ii) = tempImg;
end

end

smoothedFramesGauss = 100*smoothedImageGauss/max(smoothedImageGauss, [], 'all');
end
```